Cr as a promoter for the In2O3-catalyzed hydrogenation of CO2 to methanol

Chemical Engineering Journal 494 (2024) 153204

Contents lists available at ScienceDirect

Chemical Engineering Journal

journal homepage: www.elsevier.com/locate/cej

Cr as a promoter for the In_2O_3-catalyzed hydrogenation of CO_2 to methanol

Liang Liu, Francesco Cannizzaro, Anouar Kaychouhi, Nikolay Kosinov, Emiel J.M. Hensen *

Laboratory of Inorganic Materials and Catalysis, Department of Chemical Engineering and Chemistry, Eindhoven University of Technology, P.O. Box 513, 5600 MB Eindhoven, the Netherlands

ARTICLE INFO

Keywords:
CO_2 hydrogenation
Methanol synthesis
Indium oxide
Chromium
Promotion

ABSTRACT

The utility of Cr as a promoter for In_2O_3 catalysts in the hydrogenation of CO_2 to methanol is investigated. Uniform precursors to binary CrO_x-In_2O_3 and ternary NiO-CrO_x-In_2O_3 catalysts are prepared by flame spray pyrolysis. For the CrO_x-In_2O_3 samples, the highest methanol rate is obtained at a Cr content of 2 mol%, exceeding the methanol rate of In_2O_3 by 55 %. With increasing Cr content, the CO_2 conversion rate does not increase, albeit the methanol selectivity decreases. Characterization of the samples supported by density functional theory calculations provides insight into the role of Cr. At low content, Cr is mainly doped into the lattice of In_2O_3, which leads to more oxygen vacancy (O_v) sites. The In_2O_3 surface sites close to Cr-oxide clusters present on the surface are also activated towards O_v formation, offsetting the decrease in O_v due to coverage of the In_2O_3 surface by Cr-oxide with increasing Cr content. Cr_2O_3 dispersed on the surface of the In_2O_3 particles suppresses sintering of In_2O_3 under reducing conditions, which is especially evident at a Cr content above 2 mol% and higher reaction temperatures. Introducing Ni to the CrO_x-In_2O_3 catalysts results in a higher methanol formation rate compared to CrO_x-In_2O_3. The methanol rate increases with the Ni content with the highest activity obtained at Ni and Cr contents of 22 mol% and 8 mol%, respectively. The optimum Ni(22)-Cr(8)-In_2O_3 catalyst displays twice the methanol rate of a Ni(22)-In_2O_3 reference. Ni and Cr play different promoting roles in achieving an increased and more stable rate of methanol formation compared to In_2O_3: Ni promotes the hydrogenation of formate and methoxy surface intermediates to methanol, while Cr results in more O_v sites and suppresses sintering of In_2O_3.

1. Introduction

CO_2 hydrogenation to methanol is expected to become an important technology in the energy transition, because methanol is a versatile energy carrier and chemical building block, contributing in this way to closing the carbon cycle [1–4]. Among the many catalysts investigated, conventional Cu-based catalysts are less preferred for CO_2 hydrogenation to methanol due to their reverse water–gas shift activity and deactivation caused by active phase sintering [5,6]. In_2O_3 stands out because of its high methanol selectivity in CO_2 hydrogenation [7]. The active sites are comprised of oxygen vacancies in the In_2O_3 surface and adjacent In-O sites, which are involved in CO_2 adsorption and H_2 dissociation, respectively [8]. For practical applications, the activity of In_2O_3 is too low and it also deactivates during CO_2 hydrogenation [9].

The use of promoters for In_2O_3 has been well investigated. Pérez-Ramírez's group systematically examined the role of transition metal promoters, such as Pd, Pt, Ru, Rh, Ir, Ag, Au, Co, and Ni, introduced by flame spray pyrolysis (FSP) on methanol formation [10]. The presence of well-dispersed In_3M or In_2M_2 ensembles (M = Pd, Rh, Pt, Ru, Ir) on the In_2O_3 surface significantly enhanced the methanol yield by facilitating homolytic H_2 dissociation. Additives like Ag and Au were found to rapidly sinter on the In_2O_3 surface, which hinders H_2 homolytic splitting. The resulting particles also obstruct the active sites of In_2O_3, explaining the strongly reduced catalytic activity in the presence of Ag and Au. It has also been observed that a too high rate of H_2 activation can have a detrimental effect on catalyst stability because of over-reduction of In_2O_3, resulting in metallic In, which is also prone to agglomeration. We also reported a similar promoting role of Ni clusters as a dopant in H_2 activation for In_2O_3 [11,12]. The same group also used density functional theory calculations to investigate the impact of single atoms (SAs) of Ni, Pd, Pt and Rh on In_2O_3 on CO_2 hydrogenation over In_2O_3, mainly confirming that CO is the main product [13].

In recent years, Zr has also emerged as a promising structural promoter, improving the thermal stability of In_2O_3. Yang et al. investigated the influence of the ZrO_2 phase on the methanol yield [14]. Among these phases, monoclinic ZrO_2 (m-ZrO_2) increased the methanol yield the

* Corresponding author.
E-mail address: e.j.m.hensen@tue.nl (E.J.M. Hensen).

https://doi.org/10.1016/j.cej.2024.153204
Received 9 February 2024; Received in revised form 21 May 2024; Accepted 15 June 2024
Available online 16 June 2024

most, which is thought to include an effect of electron transfer from monoclinic ZrO_2 to In_2O_3. The resulting electron-rich In_2O_3 phase exhibits enhanced H_2 dissociation and hydrogenation activity of surface intermediates toward methanol [14]. Zhang et al. showed that specific InO_x species on m-ZrO_2 play an important role in methanol formation [15], emphasizing that the dynamic behavior of In_2O_3 on m-ZrO_2 surface with temperature can affect the product distribution. It was observed that, at high temperatures (~400 °C), In was included in m-ZrO_2, forming a solid solution in which In cations are present in the surface region of the zirconia support. This transformation lowers the number of active sites and, thus, the catalytic activity. The resulting catalyst showed a relatively high activity in the reverse water–gas shift reaction. By correlating the catalytic performance to the extent of In_2O_3 reduction, it was found that a In_2O_3/m-ZrO_2 composite containing ~ 7 wt% In has the highest methanol rate at a reaction temperature 300 °C, which was explained by optimum coverage with an InO_x surface phase.

Besides ZrO_2, the oxides of Al and Cr are also frequently used to structurally stabilize catalysts. For instance, Cr is a typical promoter in Fe-oxide catalysts used for the high-temperature water–gas shift (WGS) reaction. The main aspects of high-temperature WGS catalysts were reviewed by Zhu and Wachs [16]. Ariëns et al. showed that doping Cr into Fe-oxides prepared by co-precipitation can decrease the particle size of the active phase (magnetite) and enhance the CO conversion [17]. It is important to note that hexavalent chromium (Cr^{6+}) is a strong carcinogen, posing a threat to both human health and the environment [18]. Exposure through inhalation and ingestion of contaminated water can lead to cancer and severe damage to human organs and skin. In contrast, trivalent chromium (Cr^{3+}) exhibits very low toxicity and serves as a nutrient for the human body [18]. Cr promotion has also been reported in the context of CO_2 hydrogenation catalysis. Wang et al. reported that Cr increased the activity in a bifunctional $InCrO_x$/SAPO-34 catalyst used in the hydrogenation of CO_2 to light olefins [19]. The incorporation of Cr resulted in more surface oxygen vacancies in InO_x and stronger binding of formate intermediates, as supported by density functional theory calculations. The Cr-promoted InO_x phase was prepared by a sol–gel method, which led to a heterogeneous dispersion of CrO_x species onto In_2O_3.

Herein, we prepared Cr-doped In_2O_3 particles in a single step using flame spray pyrolysis, which brings benefits in terms of control over the In_2O_3 particle size and homogeneous dispersion of the dopant [20,21]. Reference samples were prepared by impregnating Cr on a In_2O_3 sample prepared by FSP. The structure of the catalysts was characterized by X-ray diffraction (XRD), transmission electron microscopy (TEM), Raman and X-ray adsorption spectroscopy (XAS) techniques. CO_2-TPD (temperature-programmed desorption) and quasi-in situ X-ray photoelectron spectroscopy (XPS) were employed to understand the promoting role of Cr in increasing the number of oxygen vacancy (O_v) sites. Density functional theory (DFT) calculations were used to reveal the role of different Cr species in O_v formation in In_2O_3. The catalytic performance of these samples was evaluated in CO_2 hydrogenation. An optimized Cr-promoted In_2O_3 catalyst was further promoted by Ni to render a highly active Ni-In_2O_3-Cr_2O_3 catalyst for CO_2 hydrogenation to methanol. In situ IR spectroscopy was used to investigate the reaction mechanism of methanol formation.

2. Experimental

2.1. Catalyst preparation

In_2O_3, CrO_x and In_2O_3-CrO_x catalysts with varying Cr molar contents (1 mol%, 2 mol%, 5 mol% and 10 mol% Cr) were synthesized by FSP using a Tethis NPS10 apparatus. The precursor solution was prepared by dissolving appropriate amounts of $In(NO_3)_3{\cdot}xH_2O$ (99.999%, Alfa Aesar) and $Cr(NO_3)_3{\cdot}9H_2O$ (99%, Sigma Aldrich) in an equivolumetric solvent mixture of ethanol (HPLC, Sigma Aldrich) and 2-ethylhexanoic acide (99%, Sigma Aldrich) at room temperature. The total metal concentration (In + Cr) was 0.15 mol/L. This precursor solution was injected into the flame at a flow rate of 1.0 mL/min. The flame was sustained by a flow of 1.5 L/min methane and 3.0 L/min oxygen. The catalyst powders were collected on a glass-fiber filter (Hahnemühle FineArt GmbH, GF6, 257 mm in diameter) placed above the FSP nozzle. The resulting samples are denoted as Cr(x)-In_2O_3, where x stands for atomic percentage of Cr metal normalized to the total metal content. For comparsion, a reference sample was prepared by wet impregnation. In_2O_3 obtained by FSP was suspended in a solution of $Cr(NO_3)_3{\cdot}9H_2O$ in 50 mL H_2O, which was stirred overnight, followed by drying in a rotary evaporator, and calcination in air at 300 °C for 3 h. The sample is denoted by Cr(2)/In_2O_3.

Ni-In_2O_3-CrO_x mixed oxides were also prepared using the same FSP method, where $Ni(NO_3)_2{\cdot}6H_2O$ (99%, Sigma Aldrich) was added to the precursor solution. All other conditions for FSP synthesis were the same as described above. The resulting samples are denoted Ni(x)-Cr(y)-In_2O_3, where x and y, respectively, stand for atomic percentage of Ni and Cr metal when normalized to the total metal content.

2.2. Characterization

The textural properties of the as-prepared catalysts were analyzed by N_2 physisorption at −196 °C using a Micrometrics TriStar II 3020 instrument. Before the measurements, the samples were pretreated at 120 °C in a nitrogen flow overnight. The Brunauer-Emmett-Teller (BET) method was used to determine the specific surface area. Cr and Ni loading were analyzed using Inductively coupled plasma optical emission spectroscopy (ICP-OES) (Ametek SPECTROBLUE EOP). Prior to measurements, samples were dissolved in an equivolumetric mixture of nitric acid and water at room temperature. The particle size distribution of as-prepared and used catalysts was analyzed by Transmission electron microscopy (TEM) using a FEI Tecnai (type Sphera) instrument operating at an acceleration voltage of 200 kV. For sample preparation, appropriate amounts of samples were dispersed in ethanol under ultrasonic exposure and deposited on holey copper grids. XRD patterns were recorded using a Bruker D2 Phaser diffractometer with Cu Kα radiation (λ= 1.5406 Å) between 10 and 90° with a step size of 0.02° at a scan rate of 0.23 s/step.

Infrared (IR) spectra were obtained using a Nicolet FT-IR spectrometer equipped with a cryogenic MCT detector. Typically, samples were diluted with ZrO_2 (prepared by flame spray pyrolysis with an injection rate of 1.0 mL/min, surface area of 204 m^2/g, tetragonal and monoclinic mixed phases) in a 1:10 ratio by mass. An amount of ca. 15 mg of diluted sample was pressed into a pellet and placed in a home-made cell equipped with CaF_2 windows for in situ measurements. The sample was pretreated in a He flow of 50 mL/min at 260 °C for 1 h. After cooling to 40 °C in He, a background spectrum was recorded. For in situ IR measurements at elevated pressure, the cell was pressurized to 10 bar in a 50 mL/min flow of 25 vol% CO_2 in H_2. The cell was then heated to 260 °C, during which IR spectra were recorded. After reaching 260 °C and a dwell of 1 h, the gas mixture was switched from CO_2/H_2 mixture ($H_2/CO_2 = 3$, 50 mL/min, 10 bar) to H_2 (50 mL/min, 1 bar). During this replacement of the gas volume in the cell, IR spectra were recorded for 1 h.

Raman spectra were recorded using a WITec UHTS300 spectrometer equipped with a WITec WMT50 confocal Raman microscope. The spectra were collected using a 532 nm laser with the laser power of 5 mW. X-ray photoelectron spectroscopy (XPS) measurements were carried out using a K-Alpha XPS instrument (Thermo Scientific) equipped with a monochromatic X-ray source (Al Kα = 1486.68 eV, 72 W, spot size of 400 μm) and a 180° double focusing hemispherical analyzer. Survey scans were measured at a constant pass energy of 200 eV and region scans at 50 eV. As-prepared samples were placed onto a double-sided carbon tape. Used samples (reaction in a CO_2 (20 vol%)/H_2(60 vol %)/N_2(20 vol%), total flow 50 mL/min, 260 °C, 30 bar, 14 h; cooling in an N_2 flow of 50 mL/min) were transferred to a glovebox and placed in a

gas-tight holder for transfer into the XPS analysis chamber to avoid air exposure. Quasi-in situ XPS was conducted in a Kratos AXIS Ultra 600 spectrometer equipped with a monochromatic Al Kα X-ray source. Region scans were recorded at a pass energy of 40 eV and survey scans at 160 eV. Typically, a powder sample was pressed into a pellet, which was placed in a Kratos high-temperature reaction cell attached to the XPS analysis chamber. Before XPS analysis, the sample was pretreated in an Ar flow (50 mL/min, 1 bar) for 1 h followed by cooling to 50 °C. The reaction was performed in a CO_2(20 vol%)/H_2(60 vol%)/Ar(20 vol%) gas flow of 50 mL/min at 1 bar at 260 °C or 300 °C for 2 h. The XPS spectra were analyzed using the CasaXPS software (version 3.2.23) and energy calibration was performed against the C 1 s peak of adventitious carbon at a binding energy of 284.8 eV.

XAS measurements at Cr and Ni K-edges were carried out at the CLÆSS beamline of the ALBA synchrotron (Barcelona, Spain). Energy selection was done with a Si(1 1 1) double-crystal monochromator. A mixture of the samples with boron nitride (BN) were pressed into thin pellets and sealed in Kapton tape in the home laboratory. Spectra were recorded at room temperature. The Cr K-edge XAS spectra were recorded in fluorescence mode using a 4-element silicon drift detector for the samples with a Cr loading of 2 mol%, while spectra of samples containing 9 mol% Cr were recorded in transmission mode. A $Cr(NO_3)_3$ sample was measured simultaneously in transmission mode for energy calibration. The Ni K-edge XAS spectra were measured in transmission mode with a Ni foil acting as a reference. Data analysis included energy calibration, normalization and fitting of the EXAFS part using the Demeter package (Athena/Artemis software). Scattering paths were calculated using the FEFF6 code based on crystal structures of Cr_2O_3, NiO, and Ni metal. A single Ni − In scattering path was included for EXAFS fitting. The amplitude reduction factor (S_0^2) was obtained by fitting the $Cr(NO_3)_3$ or Ni foil reference under the same conditions. The distance (ΔR), coordination number (CN), and Debye-Waller factor (σ^2) were fitted. The Fourier-transformed EXAFS spectra will be displayed without phase-correction.

Cr L-edge and O K-edge NEXAFS (Near-edge X-ray absorption fine structure) analysis was performed at the RIXS station of the SPECIES beamline at the MAX IV Laboratory (Lund, Sweden). A plane-grating monochromator illuminated with collimated light (cPGM) was used for energy selection. A retractable photodiode detector was placed in the main chamber to collect NEXAFS spectra in total fluorescence yield (TFY) mode. Before the measurements, the samples were diluted with boron nitride (BN) in a 1:5 ratio by mass, pressed into self-standing pellets and placed on an ultra-high-stable four-axis ultra-high-vacuum (UHV) manipulator using double-sided carbon tape (SPI supplies). Spectra were recorded at room temperature in UHV using an X-ray beam with vertical polarization.

Temperature-programmed reduction (H_2-TPR) measurements were performed in a Micromeritics AutoChem II setup. Typically, about 50 mg of sample was loaded into a quartz U-tube between two quartz wool layers. The sample was pretreated in a He flow (50 mL/min) at 120 °C for 1 h. TPR profiles were recorded by heating the sample from 40 to 800 °C at a rate of 10 °C/min in a 50 mL/min flow of 4 vol% H_2 in He. H_2 consumption was monitored by a thermal conductivity detector (TCD). Calibration of the TCD signal was done using a CuO reference sample. The CO_2 adsorption capacity of the as-prepared samples was determined by temperature-programmed desorption (CO_2-TPD) using a plug flow setup coupled with a mass spectrometer (Balzers TPG251). Before the CO_2-TPD analysis, the samples were pretreated in a reaction mixture flow ($CO_2/H_2/N_2$ = 10:30:10 mL/min, 30 bar) at 260 °C for 12 h, followed by a switch to a mixture of H_2 and N_2 (H_2/N_2 = 30:20 mL/min) at 260 °C. Subsequently, the samples were sealed with two three-way valves and transferred to a glovebox. They were then loaded into a quartz reactor without air exposure for CO_2-TPD experiments. CO_2 adsorption was carried out in pure CO_2 (30 mL/min) at 50 °C for 2 h. Then, the reactor was purged with He for 1 h to remove the weakly adsorbed CO_2. The TPD step involved heating in a He flow of 30 mL/min from 50 to 600 °C at a 10 °C/min rate. The amount of desorbed CO_2 was quantified by integrating the area of the corresponding desorption profile. The amount of desorbed CO_2 was calibrated by decomposition of $MgCO_3$. In CO_2 + H_2-TPD experiments, samples were pretreated in He (50 mL/min) at 260 °C for 1 h. The feed gas was then switched to a mixture of CO_2 and H_2 (CO_2/H_2 = 12.5:37.5 mL/min, 1 bar) at 260 °C for 2 h. After cooling to 40 °C, the feedstock was switched back to He (30 mL/min). The TPD step followed the same procedure as described above.

2.3. Catalytic activity measurements

High-pressure CO_2 hydrogenation tests were carried out in a down-flow stainless-steel reactor (ID = 4 mm). Typically, the catalyst was pressed, crushed and sieved into a 125–250 μm fraction, loaded into the reactor (100 mg) and pretreated in a He flow of 50 mL/min at 260 °C using a rate of 5 °C/min at 1 bar, followed by a dwell of 1 h. The catalyst was then exposed to the reaction mixture flow ($CO_2/H_2/N_2$ = 10:30:10 mL/min), followed by an increase of the pressure to 30 bar using a back-pressure regulator. The reaction was initially tested at 260 °C and subsequently at 300 °C. To prevent condensation of reaction products, the stainless-steel tubes downstream of the reactor were heated to 130 °C. The product composition was analyzed by an online gas chromatograph (Interscience CompactGC) equipped with Rtx-1 (FID), Rt-QBond and Molsieve 5A (TCD), and Rt-QBond (TCD) columns. Response factors $f(i)$ for each compound i, respective to the internal standard of nitrogen, in the GC analysis were determined by Eq. 1:

$$f(i) = \frac{\mathrm{A}(i) \times F(\mathrm{N_2})_{\mathrm{in}}}{\mathrm{A}(\mathrm{N_2}) \times F(i)_{\mathrm{in}}} \quad (1)$$

where A(i) is the integrated area determined for the peak of compound i, and $F(i)_{\mathrm{in}}$ is the corresponding known volumetric flow rate at the reactor inlet. The unknown effluent volumetric flow rate of product was determined using Eq. 2:

$$F(i)_{\mathrm{out}} = \frac{\mathrm{A}(i)}{\mathrm{A}(\mathrm{N_2}) \times f(i)} \times F(\mathrm{N_2})_{\mathrm{out}} \quad (2)$$

The CO_2 conversion (X), product selectivity (S) and methanol formation rate (STY) were calculated using the following equations:

$$X(\mathrm{CO_2}) = \frac{F(CO)_{\mathrm{out}} + F(\mathrm{CH_3OH})_{\mathrm{out}} + F(\mathrm{CH_4})_{\mathrm{out}}}{F(\mathrm{CO_2})_{\mathrm{out}} + F(\mathrm{CO})_{\mathrm{out}} + F(\mathrm{CH_3OH})_{\mathrm{out}} + F(\mathrm{CH_4})_{\mathrm{out}}} \quad (3)$$

$$S(\mathrm{product}) = \frac{F(\mathrm{product})_{\mathrm{out}}}{F(CO)_{\mathrm{out}} + F(\mathrm{CH_3OH})_{\mathrm{out}} + F(\mathrm{CH_4})_{\mathrm{out}}} \quad (4)$$

$$STY(\mathrm{CH_3OH}) = \frac{F(\mathrm{CH_3OH})_{\mathrm{out}} \times Mw(\mathrm{CH_3OH})}{V_m \times m_{\mathrm{cat}}} \quad (5)$$

where F stands for the volumetric flow rate determined based on the N_2 internal standard using calibrated response factors, M_w(CH_3OH) is the molecular weight of methanol and V_m is the molar volume of ideal gas at standard conditions.

2.4. Density functional theory calculations

Density functional theory (DFT) calculations were conducted using the projector augmented wave (PAW) method [22] and the Perdew–Burke–Ernzerhof (PBE) [23] exchange–correlation functional as implemented in the Vienna Ab Initio Simulation Package (VASP) software [24,25]. The valence 5s and 5p states of In were treated explicitly as valence states within the scalar-relativistic PAW approach. To find solutions to the Kohn-Sham equations, we employed a plane-wave basis set with a cut-off energy of 400 eV. The Brillouin zone was sampled using a 3 × 3 × 1 Monkhorst-Pack grid. All calculations were spin-

polarized. Gaussian smearing (σ = 0.1 eV) was employed.

The In_2O_3(1 1 1) surface termination was chosen as a support for Cr species, as it is more stable than the (1 1 0) and (1 0 0) surfaces, as shown in a previous computational study [26]. The stoichiometric In_2O_3(1 1 1) surface consists of a three-dimensional slab with periodic boundary conditions. We introduced a 15.0 Å vacuum region in the direction perpendicular to the surface (*c*-direction) to avoid spurious interactions between neighboring cells. The upper two layers were allowed to move, whereas the bottom two were frozen. The supercell had dimensions of 14.57 Å × 14.57 Å × 26.01 Å and contained 96 O atoms and 64 In atoms, distributed in four atomic layers. We also verified that the electron density approached zero at the edges of the periodic super cell in the *c*-direction. A structural model for a single atom (SA) of Cr (denoted by Cr-In_2O_3) was evaluated from a set of structures in which surface In atoms were replaced one at a time by Cr atoms. The most stable model was chosen by determining the substitution energies for each model, as defined earlier [12,13]. Several Cr-oxide clusters, each comprising 6 Cr atoms, supported on the In_2O_3(1 1 1) surface were generated by hand, followed by geometry optimization. The electronic energies of gaseous H_2, H_2O, and CO_2 were calculated using an cubic unit cell (8 × 8 × 8 $Å^3$) using a 1 × 1 × 1 Monkhorst-Pack grid (Γ-point only). Gaussian smearing was employed. The electronic energies of the surface models were corrected for zero-point energies (ZPE) of adsorbates. The ZPE correction was also employed to the energies computed for the gas-phase molecules.

The influence of oxygen vacancies on the reaction energetics in the CrO_x-In_2O_3 models was investigated by removing oxygen atoms from the In_2O_3(1 1 1) lattice and the CrO_x clusters. We used H_2O as reference to calculate the energy required to remove a surface oxygen to form a vacancy according to Eq. (6):

$$\Delta E_{O_v} = E_{\text{defective slab}} - E_{\text{stoichiometric slab}} + E_{H_2O} - E_{H_2} \quad (6)$$

where $E_{\text{defective slab}}$ is the electronic energy of the catalyst containing an oxygen vacancy, $E_{\text{stoichiometric slab}}$ is the reference energy of the stoichiometric slab, E_{H_2O} and E_{H_2} are the electronic energies of gas-phase H_2O and H_2, respectively.

We determined stable and transition states for the different models relevant to the formation of O_v via removal of H_2O. Stable states were calculated using the conjugate-gradient algorithm, while the climbing-image nudged elastic band (CI-NEB) method was employed to find candidate transition states [27]. A frequency analysis was performed to confirm the occurrence of stable and transition states. It was verified that stable states have no imaginary frequencies and transition states have a single imaginary frequency in the direction of the reaction coordinate [28]. The mass-weighted Hessian matrix in this frequency analysis was constructed using a finite difference approach with a step size of 0.015 Å for displacement of individual atoms along each Cartesian coordinate. The corresponding normal mode vibrations were also used to calculate the ZPE correction and the vibrational partition functions.

3. Results and discussion

3.1. Characterization as-prepared In_2O_3-CrO_x

The XRD patterns of the as-prepared Cr-In_2O_3 and In_2O_3 samples feature the typical diffraction lines of cubic In_2O_3 (Fig. 1a). No XRD diffraction lines related to Cr-containing phases were observed, indicating a high Cr dispersion. There were no systematic trends in the very small shifts in the positions of the diffraction lines. Therefore, from these data we cannot conclude whether the isomorphous substitution of In by Cr in In_2O_3 took place. Impregnation of Cr on a In_2O_3 sample prepared by FSP (denoted as Cr(2)/In_2O_3) resulted in sharper diffraction lines of the In_2O_3 phase, when compared to the Cr(2)-In_2O_3 at the same Cr content. This means that some agglomeration of In_2O_3 occurred during the preparation steps of the Cr(2)/In_2O_3 sample. The In_2O_3 particle size was estimated by using the Scherrer equation (Table 1). This analysis revealed a slight decrease of the particle size in the Cr-doped samples as compared to In_2O_3. While In_2O_3 has on average 5.6 nm particles, the average particle size of Cr(10)-In_2O_3 is 4.6 nm. The morphology and

Table 1
Physicochemical properties of the as-prepared and used In_2O_3-CrO_x samples.

Sample	d_{XRD} (nm)[a]	Specific surface area ($m^2 \cdot g^{-1}$)	d_{XRD} (nm)[a]	Specific surface area ($m^2 \cdot g^{-1}$)
	As-prepared[b]		Used[c]	
In_2O_3	5.6	150	12.5	67
Cr(1)-In_2O_3	5.0	162	9.9	54
Cr(2)-In_2O_3	5.0	140	11.0	60
Cr(5)-In_2O_3	5.2	135	9.3	80
Cr(10)-In_2O_3	4.6	119	6.3	95
Cr(2)/In_2O_3	5.8	85	7.7	53

[a] Particle size based on XRD line broadening and Scherrer equation.
[b] As-prepared samples prepared by FSP.
[c] After CO_2 hydrogenation (300 °C, 30 bar, $CO_2/H_2/N_2$ = 10/30/10 mL/min, 14 h).

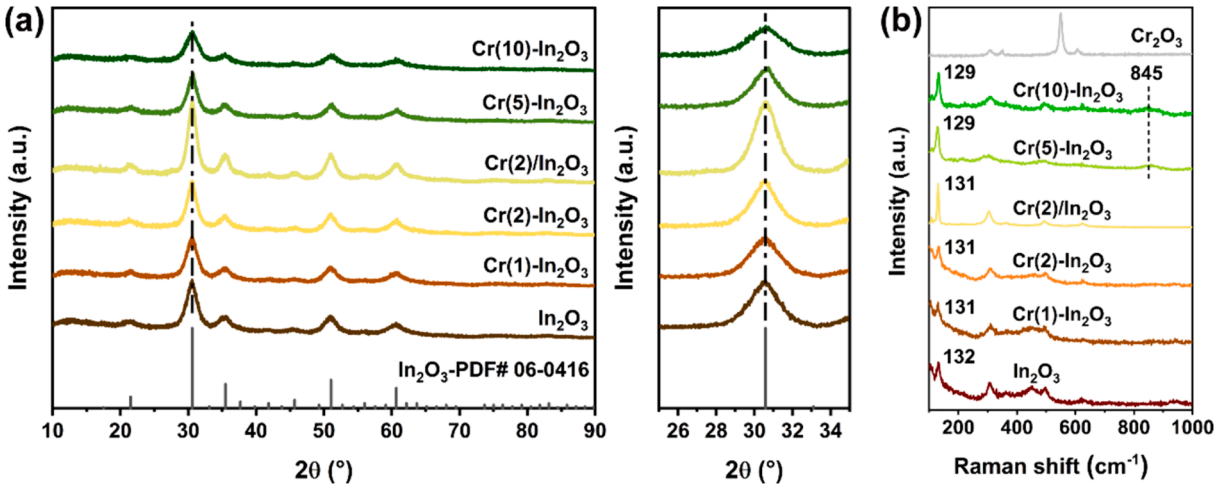

Fig. 1. (a) XRD patterns and (b) Raman spectra of the as-prepared In_2O_3-CrO_x samples.

particle size of In_2O_3-CrO_x samples were investigated by TEM (Fig. S1). All the FSP-prepared Cr-In_2O_3 samples exhibit a similar morphology consisting of globular nanoparticles with a comparable particle size distribution centered at 4–5 nm. According to TEM, the average particle size of the impregnated Cr(2)/In_2O_3 sample was 5.2 nm, which is larger than the average size of the FSP-prepared Cr(2)-In_2O_3 sample. The specific surface area of the FSP-prepared samples ranges from 119 to 162 m^2/g (Table 1). Samples with a higher Cr loading have a lower surface area, which can be related to the small interparticle voids being filled by Cr species. The surface area of the Cr(2)/In_2O_3 sample is only half of the surface area measured for Cr(2)-In_2O_3. This decrease can be mainly attributed to the presence of larger In_2O_3 particles.

Raman spectroscopy was used to study the In_2O_3-CrO_x samples (Fig. 1b). The peaks at 132, 307 and 497 cm^{-1} can be assigned to the In-O vibrations of InO_6 structural motifs.[14] The peak at 365 cm^{-1} corresponds to an In-O-In stretching vibration [14,29,30]. The peak observed at 132 cm^{-1} in the In_2O_3 sample broadens and shifts to lower wavenumbers with increasing Cr content. These changes point to a distortion in the local coordination environment of In^{3+}, caused by the incorporation of Cr^{3+} ions into the lattice of In_2O_3 [19]. In the samples with higher Cr content (≥5 mol%), a broad peak emerges at ~845 cm^{-1}, which corresponds to surface tetrahedral Cr-O species CrO_x [19,31,32], and indicates the presence of small CrO_x clusters on the In_2O_3 surface. Moreover, the peaks were sharper in the impregnated sample compared to Cr(2)-In_2O_3, which implies a higher crystallinity of In_2O_3. This is in line with the other characterization results of this sample.

The reducibility of the as-prepared In_2O_3-CrO_x samples was investigated by H_2-TPR (Fig. 2). The reduction feature at low temperature range can be assigned to the reduction of the surface of In_2O_3, which leads to the formation of O_v [7]. The high-temperature feature can be assigned to reduction of bulk In_2O_3 [31]. Reduction of Cr_2O_3 only occurs at temperatures above 1000 °C [33], while Cr^{6+} species reduce at lower temperature. Although the as-prepared samples contain small amounts of Cr^{6+} as will be shown by XPS below, the H_2-TPR profiles lack clear reduction peaks due to Cr^{6+} reduction.

Surface reduction of In_2O_3 occurred at a lower temperature in the samples with low Cr content (≤2 mol%), suggesting facile formation of O_v. The surface reduction feature shifts to a higher temperature again, as the Cr content exceeds 5 mol%. This is tentatively explained by the formation of small CrO_x clusters on the In_2O_3 surface at higher Cr content, as supported by the Raman results. Values of the H_2 consumption related to surface reduction normalized to the catalyst weight are summarized in Table S1. The effect of Cr on the surface reducibility follows from the H_2 consumption related to the low-temperature reduction peak. The H_2 consumption increases from 0.40 mmol/g_{cat} for In_2O_3 to 0.80 mmol/g_{cat} for Cr(2)-In_2O_3 and 0.98 mmol/g_{cat} for Cr(10)-In_2O_3. The value for the impregnated Cr(2)/In_2O_3 sample of 0.31 mmol/g_{cat} is lower than that of Cr(2)-In_2O_3 prepared by FSP. Notably, the H_2 consumption for In_2O_3 with a particle size of ~5 nm is almost 10 times higher than the value of 0.042 mmol/g_{cat} for In_2O_3 with a particle size of ~9 nm [11]. This points to a higher reducibility of smaller In_2O_3 crystallites. Such a strong influence of crystallite size has also been reported for CeO_2 crystallites with a size of 4–15 nm [34]. From the above, it can be stated that the inclusion of Cr in In_2O_3 using FSP enhances the reducibility of the In_2O_3 surface. This can be due to the destabilization of the In_2O_3 lattice by Cr dopants, but an effect of the crystallite size should also be considered. At higher Cr content, there can also be a stabilizing effect of CrO_x species on In_2O_3, explaining the smaller size of the In_2O_3 particles. As observed earlier for In_2O_3-Al_2O_3 samples prepared in a similar manner [35], the interface between In_2O_3 and a surface oxide phase can result in a broader temperature range of In_2O_3 reduction.

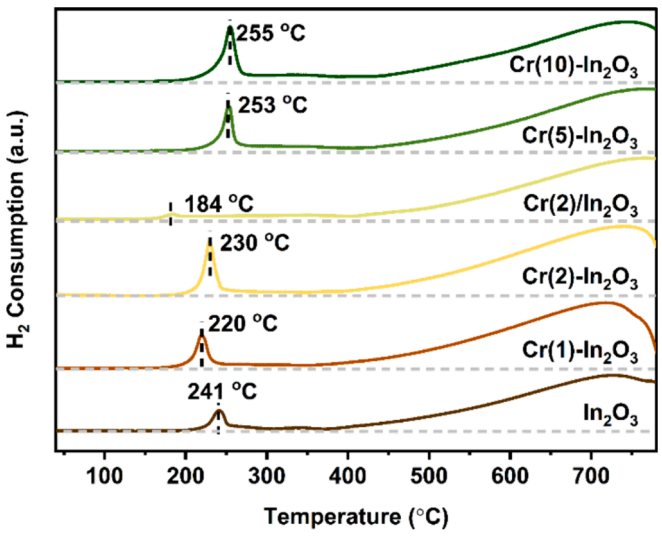

Fig. 2. H_2-TPR profiles of In_2O_3-CrO_x samples.

The composition and oxidation state of the surface of the as-prepared In_2O_3-CrO_x samples were investigated by XPS. Fig. 3 presents Cr 2p and O 1s XPS spectra of the In_2O_3-CrO_x samples. The Cr $2p_{3/2}$ peak at 576.6 eV corresponds to Cr^{3+}, while the Cr $2p_{3/2}$ peak at 579.1 eV is due to Cr^{6+} [36]. The Cr^{6+} contribution in the as-prepared samples increases from 28% for Cr(1)-In_2O_3 to 46% for Cr(10)-In_2O_3, which is likely due to the increasing contribution of surface CrO_x species (Table S2). The In 3d XPS spectra are dominated by the In $3d_{5/2}$ peak at 444.3 eV due to In_2O_3 (Fig. S2). Compared to In_2O_3, all Cr-containing samples display a minor shift of this feature to lower binding energies. Wang et al. attributed a similar shift for In_2O_3-CrO_x catalysts to the strong interactions between In and Cr in their oxide form [19]. The O 1s XPS spectra can provide information about the nature of surface oxygen species. The O 1s region of these samples can be deconvoluted into three contributions (Fig. 3b). The main peak at ~529.7 eV is assigned to lattice oxygen atoms, while the peak at ~531.9 eV is due to oxygen atoms of hydroxyl groups [7]. The assignment of the peak at ~531.1 eV is less clear, as it can be due to O atoms near O_v sites or O atoms of surface carbonates [37]. From the C 1s spectra, which can be deconvoluted into four components at 284.8, 287.5, 288.5 and 289.3 eV due to C–C, C=O, O–C=O and carbonate groups (Fig. S2) [38], it follows that the surface contains carbonates. Following a procedure from the literature [39], we estimated the amount of O_v by removing the carbonate contribution from the O 1 s spectra using the C 1 s feature at ~289.5 eV due to carbonate and assuming an O/C ratio of 3. The resulting fraction of O_v at the surface increases from 22% for In_2O_3 to a maximum value of 27% for Cr(2)-In_2O_3, followed by a nearly unchanged fraction for the samples with a higher Cr content (Table S3). The Cr(2)/In_2O_3 sample also contains slightly more O_v (24%) than In_2O_3, yet less than Cr(2)-In_2O_3. Notably, the fraction of O_v in In_2O_3 in this work is higher than the fraction of ~10 % typically reported in the literature, which may be attributed to differences in In_2O_3 particle size.

The Cr valence and electronic structure was investigated by NEXAFS for the as-prepared In_2O_3-CrO_x samples (Fig. S3a). The Cr L-edge positions in Cr(2)-In_2O_3 and Cr(10)-In_2O_3 samples are shifted to higher energies as compared to Cr_2O_3, indicating the presence Cr species with a higher oxidation state than +3 [40], which is in agreement with presence of Cr^{6+} according to XPS. Fig. S3b shows the normalized O K-edge spectra of the In_2O_3-CrO_x samples, which reflect the electronic transitions from the O 1s orbital to unoccupied states with O 2p character hybridized with In 3d [40–42]. The observation that the shape of the O K-edge feature of Cr(2)-In_2O_3 and Cr(10)-In_2O_3 is different from the one of Cr_2O_3 points to a different structure of Cr species, which is likely due to the high dispersion of Cr in contact with In_2O_3. In addition, the broad peak observed in the In_2O_3-CrO_x samples is split up due to the presence of t_{2g} and e_g orbitals. As shown before, the intensity ratio of the t_{2g} and e_g components can be correlated to the number of O_v [43]. The I_{eg}/I_{t2g} peak ratio for Cr(2)-In_2O_3 and Cr(10)-In_2O_3 are comparable, indicating a similar O_v density, which agrees with the XPS findings.

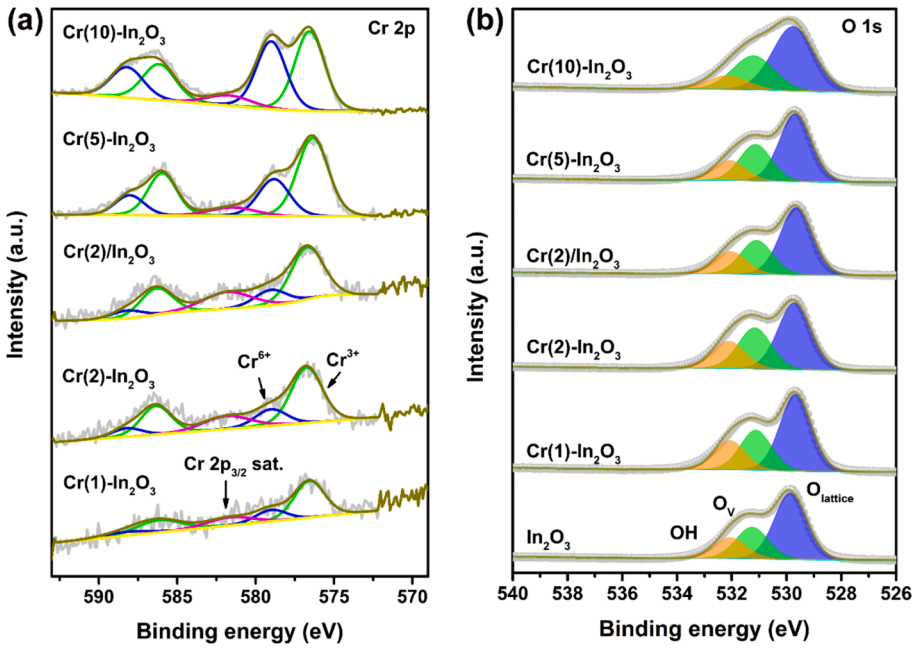

Fig. 3. (a) Cr 2p and (b) O 1s XPS spectra of the as-prepared In_2O_3-CrO_x samples.

Taken together, the characterization data above show that Cr species is present in the In_2O_3-CrO_x samples as doped cations in the In_2O_3 lattice and as highly dispersed CrO_x on the In_2O_3 surface. The addition of Cr to In_2O_3 leads to a higher O_v concentration.

3.2. Catalytic performance

The catalytic performance of the In_2O_3-CrO_x samples was evaluated at a pressure of 30 bar and a H_2/CO_2 molar ratio of 3 (Fig. 4). The CO_2 conversion was kept below 10%. Fig. 4a shows that the CO_2 conversion at 260 °C increases with the Cr content up to a value of ca. 1.5% for Cr (2)-In_2O_3, indicating a promoting effect of Cr. With increasing Cr content, the CO_2 conversion remains nearly the same. The methanol selectivity for In_2O_3, Cr(1)-In_2O_3 and Cr(2)- In_2O_3 is nearly constant at ~60%, while a further increase of the Cr content leads to a slightly lower methanol selectivity. At a reaction temperature of 300 °C, the CO_2

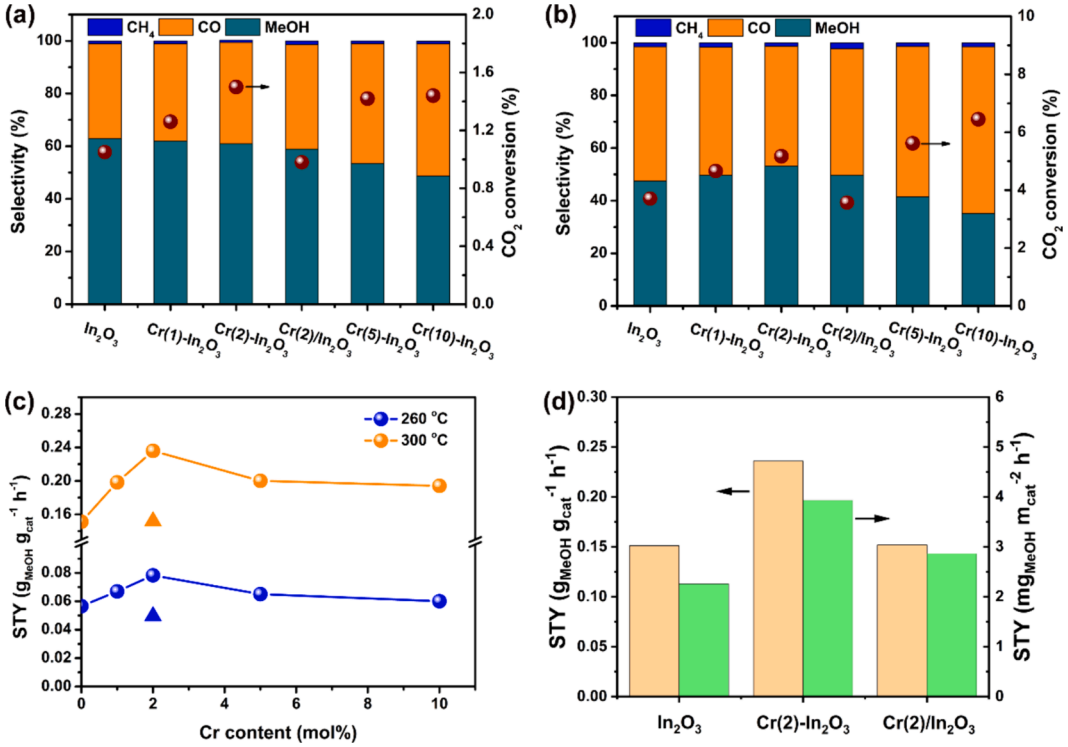

Fig. 4. CO_2 conversion and product distribution at (a) 260 °C, (b) 300 °C, and (c) methanol space–time yield (STY) as a function of the Cr content on In_2O_3 (methanol STY of Cr(2)/In_2O_3 is shown by triangles); (d) Weight and surface-area-normalized methanol space–time yield (STY) for In_2O_3, Cr(2)-In_2O_3, and Cr(2)/In_2O_3 catalysts at 300 °C. Reaction conditions: P = 30 bar, H_2:CO_2 = 3, and WHSV = 30000 mL h^{-1} g_{cat}^{-1}.

conversion is highest at 6.5% for Cr(10)-In_2O_3, which is substantially higher than the value of 3.7% for In_2O_3. The trend in the methanol selectivity at 300 °C is similar to the trend observed at 260 °C (Fig. 4b). At both reaction temperatures, the CO_2 conversion of the Cr(2)/In_2O_3 was significantly lower than that of Cr(2)-In_2O_3, albeit that the methanol selectivity was comparable. The highest methanol yield of 0.24 g_{MeOH} g_{cat}^{-1} h^{-1} was obtained with the Cr(2)-In_2O_3 catalyst at 300 °C (Fig. 4c). Fig. 4d reports the methanol formation rates at 300 °C normalized by surface area for In_2O_3, Cr(2)-In_2O_3 and Cr(2)/In_2O_3. These findings show that Cr promotion is more effective when Cr is introduced during FSP synthesis.

Fig. 5 shows the stability of In_2O_3 and Cr(2)-In_2O_3 during CO_2 hydrogenation at 260 °C. While the In_2O_3 catalyst lost about one third of its initial activity after 60 h, the decrease for Cr(2)-In_2O_3 catalyst was only 12%. The methanol formation rate of Cr(2)-In_2O_3 and In_2O_3 decreased ~10% and ~25%, respectively, during the reaction. These results point to an improved stability due to Cr. Fig. S4 shows the performance of all catalysts at 300 °C for 10 h. It can be seen that, under these more demanding conditions, the activity of In_2O_3 decreases much stronger compared to the Cr-containing catalysts. The methanol rate is much more stable for the catalysts with a Cr content of 2% and higher. Thus, Cr acts as a promoter for methanol formation and also suppresses deactivation.

3.3. Characterization used In_2O_3-CrO_x

Fig. S5 shows the XRD patterns for the used In_2O_3-CrO_x catalysts. The absence of diffraction peaks due to Cr-oxides indicates that extensive sintering of Cr did not occur during CO_2 hydrogenation. The narrower In_2O_3 diffraction lines of the used samples compared to the as-prepared samples indicates sintering of the In_2O_3 particles. Whereas no significant shift was observed between Cr(10)-In_2O_3 and In_2O_3 in the as-prepared state, the sharper lines of the used samples allow resolving small shifts and the doping Cr^{3+} ions in the In_2O_3 lattice. The small shifts to higher angles can be explained by the slightly smaller ion radius of Cr^{3+} (0.62 Å) compared to the radius of In^{3+} (0.80 Å) [44]. While the particle size of used In_2O_3 of 12.5 nm is nearly twice the size of the as-prepared In_2O_3 particles (Table 1), we observe that the extent of sintering of the Cr-containing samples is less and decreases with increasing Cr content. However, the particle size of used Cr(2)-In_2O_3 is slightly larger than the particle sizes of Cr(1)-In_2O_3 and Cr(5)-In_2O_3, thus deviating from the general trend. This could be due to an upper limit in the amount doped Cr^{3+} that can be doped in the lattice of In_2O_3. Doped Cr^{3+} distorts the lattice of In_2O_3 and facilitates the reduction of the surface In_2O_3, resulting in particle agglomeration. Cr(10)-In_2O_3 presents the smallest increase in particle size, which is consistent with the highest stability during CO_2 hydrogenation at 300 °C. Also, the Cr(2)/In_2O_3 exhibits a better resistance against sintering compared to Cr(2)-In_2O_3, suggesting that the stabilization is due to surface Cr-oxides. This is also consistent with the effect of Cr content on the stability, as characterization shows accumulation of surface CrO_x species on the In_2O_3 surface with increasing Cr content. The differences in the surface areas in Table 1 are consistent with the variations in In_2O_3 particle size. TEM analysis confirms that In_2O_3 particles are more stable, when they contain more Cr (Fig. S6). The Raman features of the used samples are qualitatively similar to those of the as-prepared samples (Fig. S7). The sharpening of the peak at 845 cm^{-1} for used Cr(5)-In_2O_3 and Cr(10)-In_2O_3 indicates that some agglomeration of CrO_x on the surface of In_2O_3 occurred during CO_2 hydrogenation.

The Cr 2p and O 1s XPS spectra of the used In_2O_3-CrO_x catalysts are shown in Fig. 6. The Cr 2p XPS spectra are given in Fig. 6a. All the used In_2O_3-CrO_x catalysts prepared by FSP contain a Cr^{6+} contribution of ~16%, which is lower than in the corresponding as-prepared samples (Table S2). This shows that some of the surface Cr^{6+} species were reduced Cr^{3+} during the reaction. The Cr^{6+} contribution of used Cr(2)/In_2O_3 is 22%, similar to the value in the as-prepared state. Fig. 6b displays the O 1s spectra of the used In_2O_3-CrO_x catalysts. Among the used In_2O_3-CrO_x catalysts, the O_v fraction in the Cr(10)-In_2O_3 catalyst reaches a maximum value of 14%. This finding is consistent with the highest H_2 consumption observed for Cr(10)-In_2O_3 by TPR, indicating that the addition of more Cr promotes oxygen vacancy formation during the reaction. The In $3d_{5/2}$ XPS spectra of the used In_2O_3-CrO_x catalysts are shown in Fig. S8. For all the used catalysts, the In $3d_{5/2}$ feature is consistently observed at 444.3 eV, signifying that In predominantly exists in the +3 oxidation state during the CO_2 hydrogenation reaction. Table S4 shows a slightly higher atomic Cr/In surface ratio for the used In_2O_3-CrO_x samples prepared by FSP when compared to the corresponding as-prepared ones. While in principle such differences can point to a higher Cr dispersion, it is more likely that some doped Cr atoms from the bulk migrated to the surface region during CO_2 hydrogenation. Instead, the Cr/In ratio for the Cr(2)/In_2O_3 sample did not change during the reaction, indicating the high structural stability of Cr species on the In_2O_3 surface.

3.4. Promoting role of Cr

Quasi-in situ XPS measurements were conducted to investigate changes in the electronic state of metal species and the O_v fraction among In_2O_3, Cr(2)-In_2O_3 and Cr(10)-In_2O_3 catalysts during CO_2 hydrogenation (CO_2/H_2/Ar = 10/30/10 mL/min, 1 bar). XPS spectra were recorded in the as-prepared state and after reaction at 260 and 300 °C for 2 h. The In 3d spectra did not change for these catalysts (Fig. S9), indicating that In remains in the +3 oxidation state. Fig. S10 shows that the Cr^{6+} contribution in the Cr-containing catalysts slightly decreased upon reaction at 260 °C. After reaction at 300 °C, the Cr^{6+} contribution decreased to 17% for Cr(2)-In_2O_3, which is higher than the value of 11% for Cr(10)-In_2O_3. This points to the higher stability of Cr^{6+} species for Cr (2)-In_2O_3.

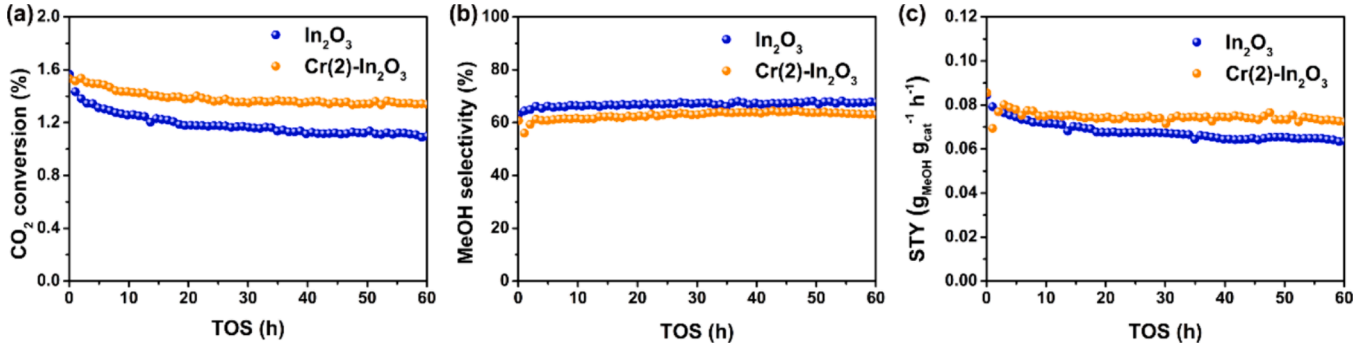

Fig. 5. Time on stream (TOS) behavior of (a) CO_2 conversion, (b) methanol selectivity and (c) methanol STY over In_2O_3 and Cr(2)-In_2O_3 catalysts. Reaction conditions: T = 260 °C, P = 30 bar, H_2:CO_2 = 3, and WHSV = 30000 mL h^{-1} g_{cat}^{-1}.

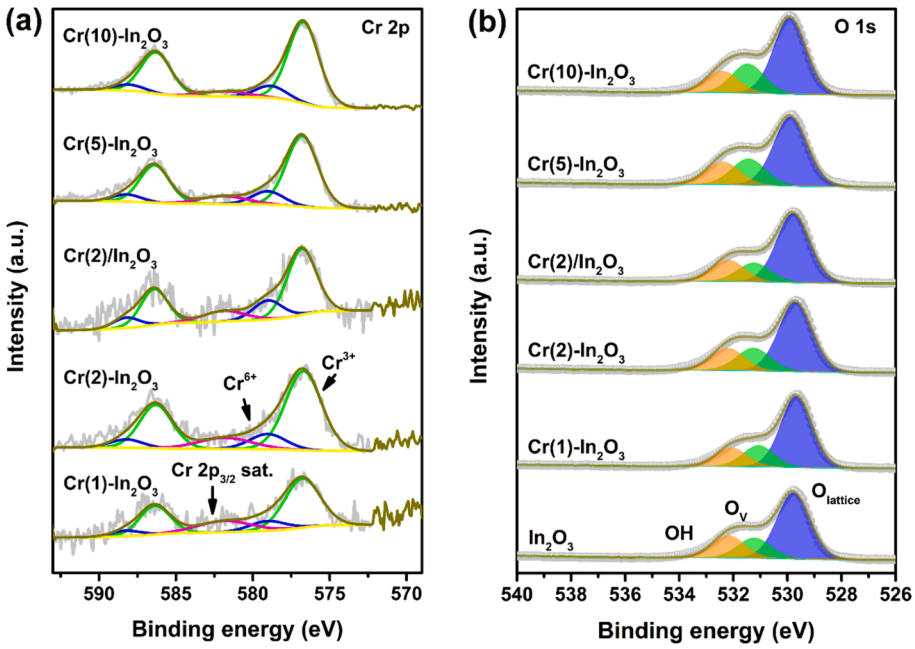

Fig. 6. (a) Cr 2p and (b) O 1s XP spectra of the used In_2O_3-CrO_x catalysts. Reaction conditions: T = 260 °C, P = 30 bar, H_2:CO_2 = 3, and WHSV = 30000 mL h^{-1} g_{cat}^{-1}.

We also studied the surface O_v fraction in these samples using O 1s XPS spectra (Fig. 7). As done above, we took into account the contributions of carbonate species in the O 1s spectra, utilizing the C 1s spectra (Fig. S11). For In_2O_3, it is observed that the O_v fraction was lower after reaction at 300 °C than after reaction at 260 °C. This is consistent with the fast deactivation of In_2O_3 at 300 °C, as supported by the catalytic results. Compared to used In_2O_3, the O_v fractions in the used Cr(2)-In_2O_3 and Cr(10)-In_2O_3 samples are higher and they are not affected by reaction at the higher temperature of 300 °C. Overall, these data suggest that Cr stabilizes the In_2O_3 particles against sintering. The smaller In_2O_3 particles cause the higher reducibility of surface In_2O_3, thereby enhancing the O_v concentration on In_2O_3.

CO_2 adsorption on the In_2O_3-CrO_x catalysts was investigated using CO_2-TPD. Prior to CO_2-TPD, the samples were evaluated in the CO_2 hydrogenation reaction (260 °C, 30 bar, $CO_2/H_2/N_2$ = 10/30/10 mL/min) for 14 h, followed by transfer without air exposure to the TPD setup and CO_2 adsorption at 50 °C. Fig. 8 displays the CO_2-TPD profiles. The peak observed around 130 °C corresponds to weakly adsorbed CO_2. In_2O_3 has few hydroxyl (OH) groups on its surface. CO_2 can weakly bind to these OH groups on the In_2O_3 surface [45]. While the peak ranging from 200 to 450 °C is attributed to CO_2 adsorbed on O_v sites [46]. With increasing Cr content above 2 mol%, this peak broadens and shifts to higher temperatures. Such changes are also seen for the Cr(2)/In_2O_3 sample. A CO_2-TPD measurement for the Cr_2O_3 reference samples showed a CO_2 desorption peak at a much higher temperature of 385 °C. XPS confirms that most Cr species are in the +3 state in the used In_2O_3-CrO_x samples. Accordingly, we speculate that the shift in the CO_2 desorption peak is caused in part by the presence of Cr_2O_3 domains on the In_2O_3 surface.

The amount of adsorbed CO_2 quantified by integrating the desorption peak in the 200 to 450 °C range increases from low values of 16.1 and 36.5 μmol/g_{cat} for In_2O_3 and Cr(1)-In_2O_3 to the highest value of

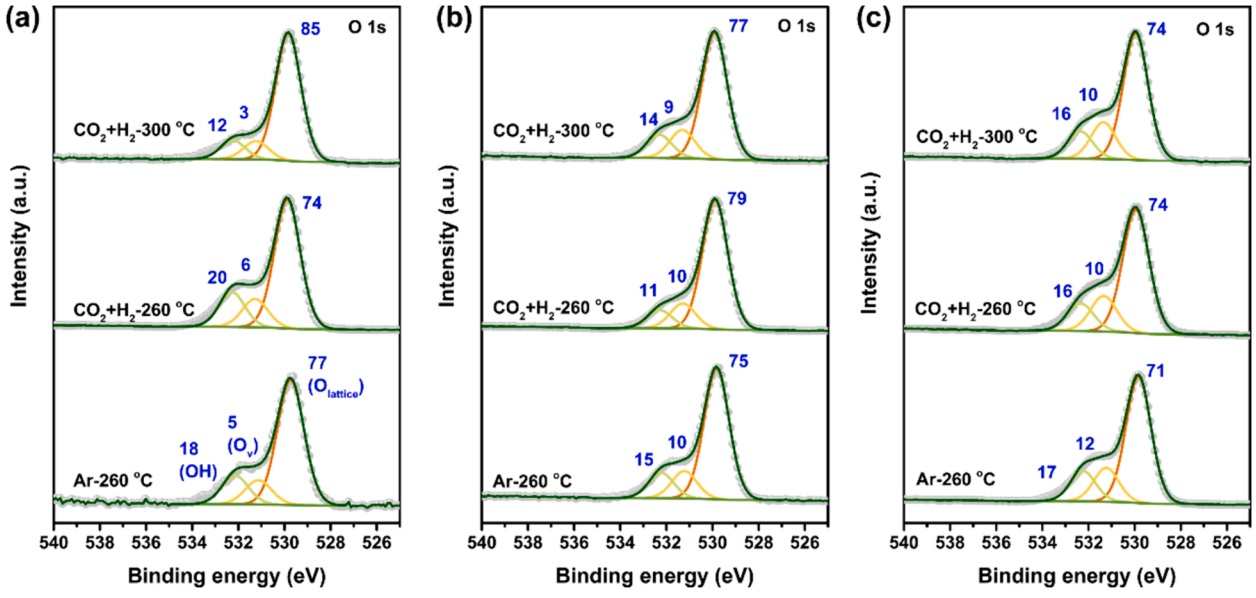

Fig. 7. O 1s XP spectra for (a) In_2O_3, (b) Cr(2)-In_2O_3 and (b) Cr(10)-In_2O_3 catalysts after treatments in various conditions.

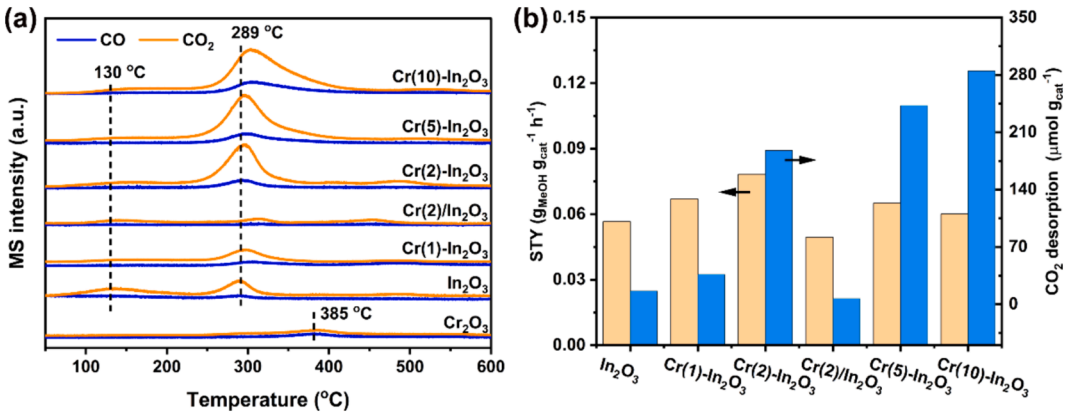

Fig. 8. (a) CO_2-TPD profiles of In_2O_3-CrO_x catalysts with different Cr content and Cr_2O_3. (b) The relation between methanol space–time yield (STY) over the In_2O_3-CrO_x catalysts during CO_2 hydrogenation at 260 °C (Fig. 4c) and the amount of CO_2 desorbed, which was obtained by quantifying the TPD desorption peak in the range of 200 to 450 °C (Table S1).

284.9 μmol/g_{cat} for Cr(10)-In_2O_3 (Table S1). The value of 7.0 μmol/g_{cat} for Cr(2)/In_2O_3 is much lower than that of 187.9 μmol/g_{cat} for Cr(2)-In_2O_3. Although a portion of CO_2 absorbed on Cr_2O_3 domains, the significantly increased CO_2 adsorption with increasing Cr content aligns with the trend in O_v fraction, suggesting enhanced formation of O_v at high Cr content. Fig. 8b shows the correlation between the amount of adsorbed CO_2 and the methanol rates. At low Cr content (≤2 mol%), the methanol rate correlates well with the CO_2 adsorbed, suggesting that the introduction of small amounts of Cr to In_2O_3 can generate more O_v and enhance CO_2 adsorption. However, as the Cr content exceeds 2 mol%, the CO_2 adsorption increases and the methanol rate decreases. This can be explained by the increasing contribution of CO_2 adsorbed on Cr-oxides at the surface, which is likely inactive in CO_2 hydrogenation to methanol. CrO_x prepared by FSP did not exhibit any CO_2 hydrogenation activity (260 °C, 30 bar, $CO_2/H_2/N_2$ = 10/30/10 mL/min). Next to CO_2 desorption, we also observed the formation of CO at the same temperature and the CO amount was seen to increase with the Cr content (Fig. 8 and Table S1). Although bulk CrO_x is not catalytically active, we still observed CO formation in In_2O_3-CrO_x samples below 300 °C during the CO_2-TPD experiments, and a higher Cr content led to more CO. This is likely related to the presence of much better dispersed CrO_x domains on the In_2O_3 surface, contributing to CO formation during both CO_2-TPD and CO_2 hydrogenation. According to the XPS, Cr^{3+} is the dominant oxidation state of Cr in the used In_2O_3-CrO_x catalysts. Therefore, we speculate that the decrease in methanol rate for samples with a high Cr content is due to the higher coverage of the In_2O_3 surface by Cr-oxide species.

Characterization revealed that Cr species are present as doped Cr atoms in the In_2O_3 lattice and as dispersed CrO_x on the In_2O_3 surface. XPS confirmed that the majority of surface Cr^{6+} species is reduced to Cr^{3+} during CO_2 hydrogenation. We employed DFT calculations to understand the role of doped and surface Cr species in O_v formation and CO_2 adsorption. The three different surface models considered are shown Fig. 9a, namely (i) the stoichiometric In_2O_3(1 1 1) surface, (ii) a Cr atom doped in the first In layer in the In_2O_3(1 1 1) surface, and (iii) a Cr_6O_9 cluster placed on the In_2O_3(1 1 1) surface. We first calculated the oxygen vacancy formation energies (ΔE_{Ov}) using Eq. (6) from section 2.4. The results are given in Fig. S12 and Table S5. The In_2O_3(1 1 1) surface contains 12 different surface O atoms, for which the oxygen vacancy formation energies (Fig. S12a and Table S5) range between −62 and +8 kJ/mol, as reported before [12,13]. Doping a Cr atom in the In_2O_3 surface makes oxygen removal slightly more difficult, with ΔE_{Ov} ranging between −38 and +66 kJ/mol (Fig. S12b and Table S5). The O atoms with the lowest ΔE_{Ov} bind to the Cr atom (oxygens 1–3 in Fig. S12b, ΔE_{Ov} = -38 kJ/mol). The Cr-O bond distance of 1.74 Å is much shorter than the original In-O bond distance at the site of doping (2.19 Å). The lattice contraction due to Cr doping brings the O atoms around the Cr dopant closer to each other than in the stoichiometric In_2O_3 case, enhancing electron–electron repulsion. This weakens the Cr-O bonds, explaining the destabilization of the O atoms around Cr. This line of reasoning is similar to the one advanced for oxygen vacancy formation for Ni-doped In_2O_3(1 1 1) [11,12]. Overall, the ΔE_{Ov} for the Cr-doped case is slightly less favorable than the most favorable ΔE_{Ov} for the stoichiometric In_2O_3 surface ($\Delta E_{Ov,Cr\text{-}doped}$ = −38 kJ/mol and ΔE_{Ov},

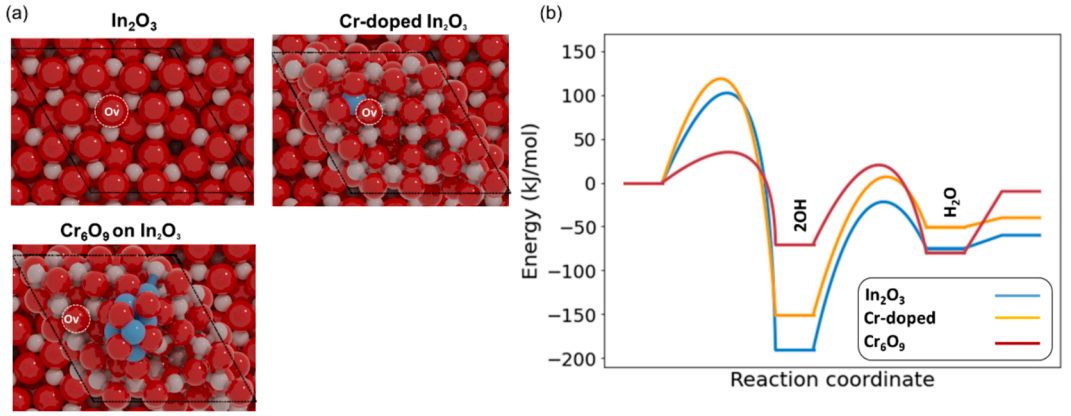

Fig. 9. (a) DFT surface models and (b) potential energy diagrams for oxygen vacancy formation via H_2O formation. The oxygens that have been removed to create a vacancy are highlighted with dashed circles (O atoms in red, In atoms in brown, and Cr atoms in blue). (For interpretation of the references to colour in this figure legend, the reader is referred to the web version of this article.)

$_{In2O3}$ = −62 kJ/mol). Nevertheless, doping Cr ions into the In_2O_3 can increase the number of oxygen vacancies, as it creates more surface sites with a favorable ΔE_{Ov}.

For the Cr_6O_9-In_2O_3 model, we considered oxygen vacancies belonging to the In_2O_3 surface and the Cr_6O_9 cluster (Fig. S12c). On In_2O_3, the ΔE_{Ov} values range between −10 and +117 kJ/mol, while higher values are found for the Cr_6O_9 cluster itself, with ΔE_{Ov} values ranging between 104 and 124 kJ/mol (Table S5). The unfavorable oxygen vacancy formation energies for the O atoms on the Cr_6O_9 cluster compared to In_2O_3 is in line with the TPR results, pointing to higher reduction temperatures for the CrO_x overlayer. Moreover, it is in keeping with the higher stability of Cr_2O_3 ($\Delta H_{f,\ 298\ K}$ = −1131.2 kJ/mol) compared to In_2O_3 ($\Delta H_{f,\ 298\ K}$ = −922.9 kJ/mol) [47,48].

CO_2 hydrogenation conditions favor a surface configuration, in which one oxygen vacancy per unit cell is exposed, as also employed as a model in previous computational reports [24]. Next, we studied the pathways of oxygen vacancy formation on the models in Fig. 9a. The potential energy diagrams for the removal of the oxygen atom with the lowest ΔE_{Ov} for each surface (O_v in Fig. 9a) are shown in Fig. 9b (data in Table S6, structures of initial, transition and finale states in Tables S7-S9). For the stoichiometric In_2O_3 surface and the Cr-doped model, homolytic dissociation of H_2 results in two OH groups (Tables S7-S8). On the In_2O_3 surface, H_2 dissociation has an activation energy of 98 kJ/mol and the reaction energy is ΔE_r = −197 kJ/mol. These values agree well with an earlier DFT study of H_2 dissociation on In_2O_3 [49]. Doping of a Cr atom in the In_2O_3 surface renders H_2 activation less favorable with activation and reaction energies of 137 and −140 kJ/mol, respectively. For the Cr_6O_9 cluster, H_2 activation (Fig. 9b and Table S9) has a relatively low activation energy of 20 kJ/mol (ΔE_r = −60 kJ/mol). The transition state involves Cr-H and O–H moiety, while the final state is characterized by one Cr-OH and an OH moiety on In_2O_3. The next step involves OH hydrogenation to H_2O via proton migration. On In_2O_3(1 1 1), this step has an activation energy of 97 kJ/mol and is endothermic by 75 kJ/mol. On Cr-doped In_2O_3, proton migration has a slightly higher activation energy of 119 kJ/mol (ΔE_r = 49 kJ/mol). Proton migration from the Cr cluster to In_2O_3 results in facile formation of H_2O on the In_2O_3. This step has an activation energy of 51 kJ/mol and is slightly exothermic (ΔE_r = −9 kJ/mol). Desorption of H_2O from In_2O_3, Cr-doped In_2O_3 and Cr_6O_9 on In_2O_3 cost 10, 10 and 63 kJ/mol, respectively. The overall barriers (in brackets reaction energies) with respect to gas-phase H_2 are 98 (−62 kJ/mol), 137 (−38 kJ/mol), 20 (−10 kJ/mol), for In_2O_3, Cr_1-dopded and Cr_6O_9. Thus, Cr doping leads to a slightly higher barrier for O removal as H_2O. This will not suppress the role of such O_v in methanol formation, as the overall barrier for O_v formation is still low compared to the overall barriers for methanol formation on In_2O_3 [21,22]. These theoretical investigations show that Cr can result in more O_v sites by replacing In^{3+} in the In_2O_3 (Cr doping) and through modifying the electronic structure of In-O-In moieties close to Cr-oxide clusters formed on the surface.

We next explored different adsorption configurations of CO_2 on the CrO_x-In_2O_3 models after O removal. The optimized structures are shown in Fig. S13. For the Cr_1-doped model, CO_2 absorption led to a surface carbonate species with two stable adsorption configurations being identified. The most stable configuration (ΔE_{ads} = −74 kJ/mol, Fig. S13a) features CO_2 adsorbed with the carbon atom close to the Cr single atom. This adsorption configuration is similar to the one observed for the In_2O_3(1 1 0) surface, which involved slightly weaker adsorption energy (ΔE_{ads} = −41 kJ/mol) [8]. The small difference in adsorption energies between In_2O_3 and Cr_1-In_2O_3 may be due to the fact that we included van der Waals corrections in our DFT calculations unlike Ye et al [8]. In the less stable position (ΔE_{ads} = −36 kJ/mol, Fig. S13b), CO_2 is further away from the Cr atom. On the Cr_6O_9 model, CO_2 adsorbs preferentially at the interface between the Cr_6O_9 cluster and In_2O_3 with one O atom filling the oxygen vacancy in the In_2O_3 surface (ΔE_{ads} = −73 kJ/mol, Fig. S13c). Adsorption on the Cr-oxide cluster with one oxygen vacancy (removing O13 from the model shown in Fig. S12) was also explored, but lead to a weaker binding compared to adsorption on In_2O_3 (ΔE_{ads} = −10 kJ/mol, Fig. S13d). In an earlier study of a Ni atom doped inside In_2O_3, the hydrogenation of carbonate to formate (HCOO*) involved a high activation barrier [12], excluding its involvement in methanol synthesis. The presence of Cr-H species upon H_2 dissociation on the Cr_6O_9 cluster can lower the barrier for the protonation of the carbon atom in adsorbed CO_2, resulting in the facile formation of HCOO*. Accordingly, we conducted CO_2 + H_2-TPD experiments on In_2O_3, Cr(2)-In_2O_3, and Cr(5)-In_2O_3 catalysts to compare their ability to activate H_2 (Fig. S14). After pretreatment in the reaction mixture (CO_2/H_2 = 12.5/37.5 mL/min, 1 bar) for 2 h, a TPD was carried out from 40 to 600 °C. The H_2 desorption peak was seen to increase with increasing Cr loading, supporting the conclusion of H_2 activation being facilitated by Cr-oxides on the In_2O_3 surface.

3.5. *Ni-Cr-In_2O_3*

Although we found that the presence of Cr as Cr-oxide species can facilitate O_v formation through facile H_2 activation, typically transition metal promoters like Pt, Pd and Ni are preferred to promote H_2 dissociation on In_2O_3 catalysts for CO_2 hydrogenation. For this purpose, Ni-In_2O_3-CrO_x samples were synthesized by FSP at various Ni and Cr contents (Table S10). The catalytic performance among In_2O_3, Cr(10)-In_2O_3, Ni(12)-In_2O_3 and Ni(12)-Cr(9)-In_2O_3 catalysts is shown in Fig. 10. Notably, Cr(10)-In_2O_3 and Ni(12)-Cr(9)-In_2O_3 catalysts were prepared at the same Cr/In atomic ratio of 1/9. Fig. 10a shows that Ni(12)-Cr(9)-In_2O_3 exhibits the highest CO_2 conversion of 5.1% at 260 °C, significantly surpassing the values of 1.0% for pure In_2O_3, 1.5% for Cr(10)-In_2O_3 and 4.3% for Ni(12)-In_2O_3. However, the methanol selectivity in Ni(12)-Cr(9)-In_2O_3 (~40%) is similar to that Ni(12)-In_2O_3, lower than those of In_2O_3 and Cr(10)-In_2O_3. Fig. 10b shows that the methanol rate of Ni(12)-In_2O_3 decreases substantially during the first 30 min on stream. In contrast, the Ni(12)-Cr(9)-In_2O_3 catalysts hardly deactivates, indicating that the stabilizing effect of Cr observed above is retained in the presence of Ni. The highest methanol rate is observed in Ni(12)-Cr(9)-In_2O_3. These findings suggest that Ni and Cr can synergistically improve CO_2 hydrogenation synthesis with In_2O_3 catalysts.

Fig. S15 shows the catalytic performance of the Ni-In_2O_3-CrO_x samples with different Ni and Cr contents in CO_2 hydrogenation. The simultaneous presence of Cr and Ni increases the CO_2 conversion. For instance, at a Ni content of 12 mol%, the addition of 2 mol% Cr increases the CO_2 conversion at 260 °C from 4.3% to 5.3%. At a Ni content of 22 mol%, the CO_2 conversion of Ni(22)-Cr(8)-In_2O_3 is nearly two times higher than that of Ni(22)-In_2O_3. The methanol selectivity does not substantially change for these catalysts. The highest CO_2 conversion at 300 °C is 15% for Ni(22)-Cr(8)-In_2O_3, which can be compared to a CO_2 conversion of 10% for Ni(22)-In_2O_3. The CO_2 conversion in Ni(22)-Cr(8)-In_2O_3 is lower than the CO_2 equilibrium conversion of ~30% under the given conditions, implying that increasing the active sites by adjusting the Ni or Cr content can further enhance the catalyst performance. The methanol selectivity in all the catalysts is comparable and below 20% at 300 °C. In Fig. S15c, the Ni(12)-Cr(9)-In_2O_3 catalyst has a 25% higher methanol rate than Ni(12)-In_2O_3 after stabilization at 260 °C. The Ni(22)-Cr(8)-In_2O_3 catalyst exhibits the highest methanol rate of 0.24 $g_{MeOH}\ g_{cat}^{-1}\ h^{-1}$, which is approximately twice that of Ni(22)-In_2O_3. At a temperature of 300 °C, Ni(12)-In_2O_3, Ni(12)-Cr(x)-In_2O_3 and Ni(22)-Cr(8)-In_2O_3 catalysts exhibit similar methanol rates with Ni(22)-In_2O_3 having a significantly lower methanol rate. These data indicate the optimal Ni and Cr contents for promoting methanol synthesis in Ni-In_2O_3-CrO_x samples. We also compared the Ni-In-Cr catalysts to other Cu-based and Ni-promoted catalysts. As shown in Table S11, Ni-In_2O_3 prepared by FSP shows a slightly lower methanol rate than a Ni-In_2O_3 sample described in the literature [45], which could be due to the lower pressure and H_2/CO_2 ratio. The methanol rate of Ni-In_2O_3-CrO_x is similar to that of Cu-based catalysts, such as Cu-ZnZr and Ce-CuZn samples [50,51].

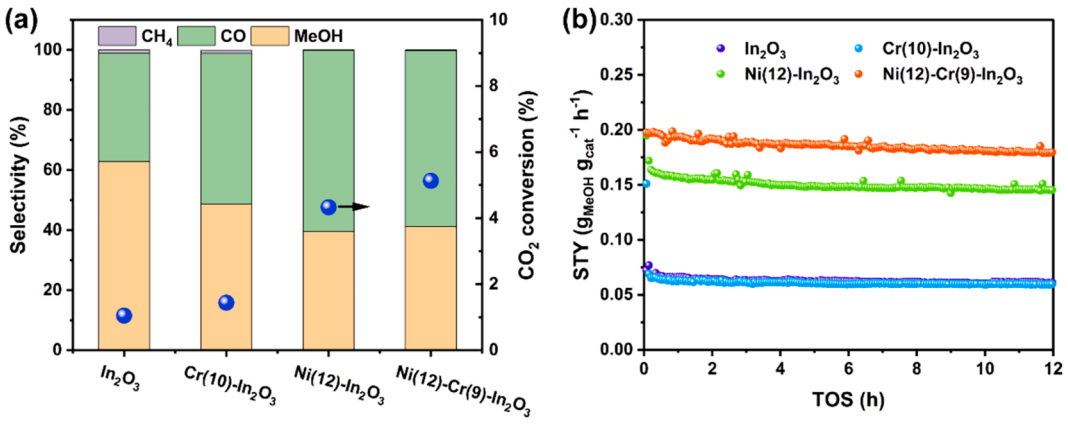

Fig. 10. (a) CO_2 conversion and product selectivity at 260 °C and (b) methanol space–time yield (STY) along with the time on stream over In_2O_3, Cr(10)-In_2O_3, Ni(12)-In_2O_3 and Ni(12)-Cr(9)-In_2O_3 catalysts. Reaction conditions: P = 30 bar, H_2:CO_2 = 3:1, and WHSV = 30000 mL h^{-1} g_{cat}^{-1}.

XRD analysis was employed to determine the phases present in the as-prepared Ni-In_2O_3-CrO_x samples (Fig. 11a). All diffraction lines of Ni(12)-In_2O_3 can be attributed to cubic In_2O_3, with peak positions shifting slightly to higher angles compared to pure In_2O_3. This shift suggests the incorporation of Ni into the In_2O_3 lattice in line with the earlier work of Zhu et al [11]. However, as the Ni content is increased to 22 mol%, the diffraction lines become broader compared to those in Ni(12)-In_2O_3, pointing to smaller In_2O_3 particles. No diffraction peaks indicative of Cr-oxides were observed for the Cr-containing samples. The average particle size for the as-prepared Ni(12)-In_2O_3 is ~3.3 nm (Table S12). The estimation of the average particle size based on the Scherrer equation for the as-prepared Ni-In_2O_3-CrO_x and Ni(22)-In_2O_3 samples cannot be realized due to the broad diffraction lines, suggesting a smaller particle size than 3.3 nm.

The XRD patterns of the used Ni-In_2O_3-CrO_x catalysts are shown in Fig. S16. The used catalysts only display diffraction peaks of In_2O_3, showing that Ni and Cr remain highly dispersed. Compared to the as-prepared catalysts, the diffraction lines due to In_2O_3 are sharper, pointing to sintering of the In_2O_3 particles during the reaction. The average size of the In_2O_3 particles in the used Ni(12)-In_2O_3 is 19.3 nm (Table S11). The In_2O_3 particle sizes in the used Ni(12)-Cr(2)-In_2O_3 and Ni(12)-Cr(9)-In_2O_3 catalysts are similar at ~17 nm. At a Ni content of 22 mol%, the In_2O_3 particle size in the used Ni(22)-In_2O_3 catalyst is 51 nm, whereas the particle size in Ni(22)-Cr(8)-In_2O_3 is smaller, i.e. 38 nm. These findings show that the stabilizing effect of Cr on In_2O_3 is retained in the presence of Ni.

H_2-TPR was used to study the reduction behavior in the Ni-In_2O_3-CrO_x samples (Fig. 11b). Ni-In_2O_3 and Ni-In_2O_3-CrO_x samples exhibit a similar peak at ~240 °C, corresponding to reduction of the In_2O_3 surface [7]. The H_2 consumption corresponding to this surface reduction amounts to 0.33 mmol/g_{cat} for Ni(12)-In_2O_3, while it is higher at 0.49 mmol/g_{cat} for Ni(12)-Cr(2)-In_2O_3 and 0.41 mmol/g_{cat} for Ni(12)-Cr(9)-In_2O_3 (Table S13). Ni(22)-In_2O_3 exhibits a lower H_2 consumption compared to Ni(12)-In_2O_3. This may be attributed to NiO clusters covering part of the In_2O_3 surface, hindering the reduction of In_2O_3 [52]. The addition of 8 mol% Cr to Ni(22)-In_2O_3 results in a significantly enhanced H_2 consumption of 0.65 mmol/g_{cat}. These results indicate that the introduction of Cr to Ni-In_2O_3 facilitates the reduction of surface In_2O_3, similar to Cr promotion of In_2O_3. The reduction feature at ~280 °C for Ni(12)-In_2O_3 is due to the NiO reduction to Ni metal [11]. This feature is located at higher temperature for the Ni(12)-Cr(9)-In_2O_3 and Ni(22)-Cr(8)-In_2O_3 samples, suggesting that Ni-oxide might preferentially interact with Cr-oxide at the surface delaying Ni reduction. The H_2/Ni ratio associated with this feature is 1.70 for Ni(12)-In_2O_3, pointing to the further reduction of In_2O_3 to In due to H_2 spillover from metallic Ni. The H_2/Ni ratio increases to 1.85 and 2.25 for Ni(12)-Cr(2)-In_2O_3 and Ni(12)-Cr(9)-In_2O_3, respectively, which may be due to reduction of Cr^{6+} species present in the as-prepared samples.

The normalized XANES spectra at the Cr K-edge are shown in Fig. 12a. The pre-edge feature located at 5993.7 eV due to the 1s to 3d transition for the CrO_x sample points to the presence of Cr^{6+} [53], which is further supported by the higher edge energy compared to the Cr_2O_3 reference. It is also in line with the high Cr^{6+} fraction of 83% in CrO_x according to XPS (Fig. S17). The as-prepared Ni(12)-Cr(2)-In_2O_3 and Ni(12)-Cr(9)-In_2O_3 samples also contain a pre-edge feature due to Cr^{6+}, while the broad feature ranging from 6010 to 6030 eV points to the presence of Cr(III) hydrate [54]. The XANES of the used Ni(12)-Cr(2)-In_2O_3 and Ni(12)-Cr(9)-In_2O_3 samples are similar to the XANES

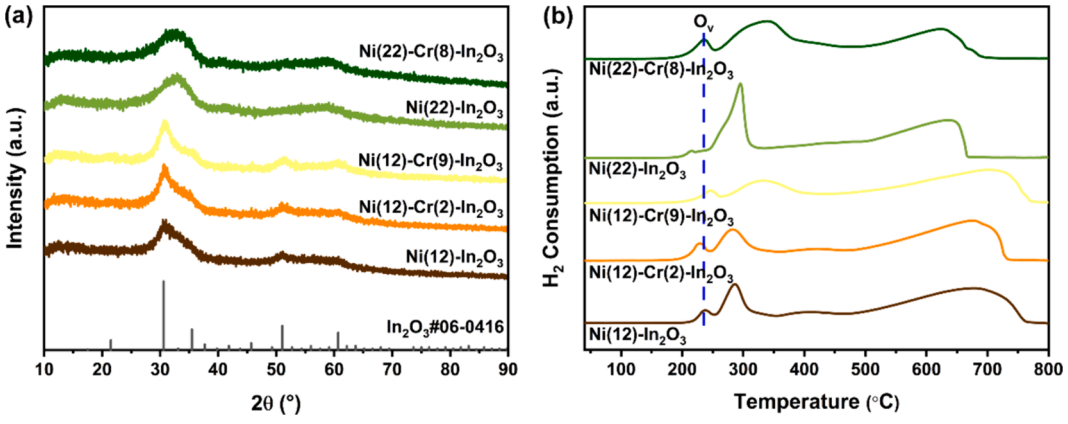

Fig. 11. (a) XRD patterns and (b) TPR profiles of the as-prepared Ni-In_2O_3-CrO_x samples.

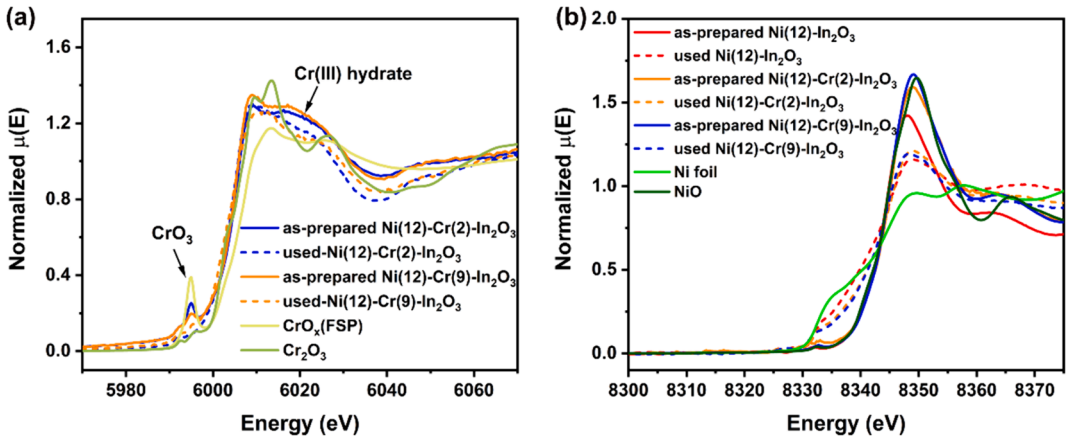

Fig. 12. Normalized XANES spectra at the (a) Cr K-edge and (b) Ni K-edge of the as-prepared and used Ni(12)-In_2O_3-CrO_x samples.

spectrum of Cr_2O_3, while the features corresponding to Cr(III) hydrate and Cr^{6+} disappeared. EXAFS spectra were obtained at Cr K-edge for as-prepared and used Ni(12)-Cr(2)-In_2O_3 and Ni(12)-Cr(9)-In_2O_3 samples (Fig. S18) and the fit results are collected in Table S14. The first and second shell at uncorrected distances of 1.6 and 2.5 Å correspond to the Cr-O and Cr-O-Cr contributions, respectively, in Cr_2O_3 reference. In the as-prepared Ni(12)-Cr(2)-In_2O_3 and Ni(12)-Cr(9)-In_2O_3 samples, only Cr-O contribution is observed, suggesting that Cr atoms are well dispersed in In_2O_3. After the reaction, the Cr-O coordination numbers decrease, while a Cr-O-Cr shell appears, indicating the clustering of Cr species on the In_2O_3 surface during the reaction. Notably, the Cr samples after the reaction show a Cr-O-Cr shell with a coordination number (CN) of ~1, which is much lower than the CNs of the Cr-O-Cr shell (~4) in bulk Cr_2O_3, pointing to highly dispersed Cr clusters on the In_2O_3 surface.

The Ni K-edge XANES of the Ni-containing samples are shown in Fig. 12b. The edge energy at 8344 eV is similar to that of the NiO reference. The edge energy of the used Ni(12)-In_2O_3 sample is ~8340 eV, indicating the reduction of NiO to metallic Ni. Nevertheless, some NiO is likely present as the edge energy of the used Ni(12)-In_2O_3 is slightly higher than the edge energy of the Ni foil. The used Ni(12)-Cr(2)-In_2O_3 and Ni(12)-Cr(9)-In_2O_3 exhibit higher edge energies than to Ni(12)-In_2O_3, indicating that the Cr-containing samples contain a larger amount of NiO. The EXAFS results show a decrease of the Ni-O and Ni-O-Ni shells after the reaction (Fig. S19, Table S15). A shell at 2.5 Å in the Ni(12)-In_2O_3 catalyst can be related to metallic Ni-In bonds [55]. In the used Ni(12)-Cr(2)-In_2O_3 and Ni(12)-Cr(9)-In_2O_3 catalysts, a Ni-Ni (metallic) shell at ~2.2 Å was observed, while the Ni-In shell was absent. This observation suggests that the introduction of Cr to Ni-In_2O_3 weakens the interaction between Ni and In in the reduced Ni species. In addition, EXAFS reveals CNs of ~2 for the metallic Ni-Ni shell in Ni-In_2O_3-CrO_x and ~2 for the metallic Ni-In shell in Ni-In_2O_3. These CNs are much lower than those expected for nanoparticles (CN > 10), suggesting a high dispersion of the Ni phase in the former samples.

We next investigated reaction intermediates of CO_2 hydrogenation by in situ IR spectroscopy for the Cr(10)-In_2O_3, Ni(12)-In_2O_3 and Ni(12)-Cr(9)-In_2O_3 samples (Fig. 13a-13c). Exposing the samples to a model reaction mixture ($H_2/CO_2 = 3$, 10 bar) at 40 °C resulted in the formation of monodentate carbonate (m-CO_3^{2-}, 1422 and 1335 cm^{-1}), bicarbonate (HCO_3^-, 1613 and 1227 cm^{-1}) and bidentate carbonates (b-CO_3^{2-}, 1633 and 1528 cm^{-1}) [56–58]. As the temperature increases, the bands due to bicarbonates disappear and the formation of polycarbonates (1484 cm^{-1}), formates (1367, 1380, 1571–1592, 2872, and 2973 cm^{-1}) and methoxy (1045, 1142, 2827, and 2931 cm^{-1}) is apparent [57]. The hydrogenation behavior of these intermediates was evaluated by switching the feed from $CO_2 + H_2$ (10 bar, 50 mL/min) to pure H_2 (1 bar, 50 mL/min) at 260 °C (Fig. 13a-13c). This led to stronger CH_3O* bands and weaker HCOO* bands, suggesting that the reaction follows the formate pathway, where HCOO* is considered as the key intermediate for methoxy and methanol formation, which is in line with suggestions from DFT calculations [12]. Overall, the evolution of the IR bands was qualitatively comparable for the three investigated samples.

The formate IR bands of the three samples were compared after 1 h CO_2 hydrogenation at 260 °C (Fig. 13d). The ν(CH) band of HCOO* in all samples is located at the same position of 2872 cm^{-1}. In Cr(10)-In_2O_3, two distinct features at 1571 and 1592 cm^{-1} in the C-O region can attributed to the O-C-O (ν_{as}(OCO)) vibration of HCOO*. The ν_{as}(OCO) band at 1571 cm^{-1} in HCOO* has been reported to represent formate on In_2O_3 [59]. The ν_{as}(OCO) band at 1592 cm^{-1} in Cr(10)-In_2O_3 is similar to the band observed in In_2O_3-Al_2O_3 samples in our previous study of Al-promoted In_2O_3 [35]. By analogy, we assign this to formate adsorbed on an oxygen vacancy close to highly dispersed Cr. In Ni(12)-In_2O_3, we also found two ν_{as}(OCO) bands of HCOO* at 1591 and 1571 cm^{-1}. The feature in the formate region at 1591 cm^{-1} can be assigned to formate on Ni sites, as this band was also observed for Ni/SiO_2 during CO_2 hydrogenation [60]. Based on the EXAFS analysis of used Ni-In_2O_3, it can be said that Ni strongly interacts with In_2O_3 during CO_2 hydrogenation. This strengthens the assignment of the 1591 cm^{-1} band to HCOO* on Ni sites close to In_2O_3. Such a formate intermediate may also involve coordination to oxygen vacancies in In_2O_3 at the Ni-In_2O_3 interface. Additionally, the formate band in Ni(12)-Cr(9)-In_2O_3 occurs at a lower wavenumber of 1573 cm^{-1}, which is comparable to the location of HCOO* on In_2O_3 and different from Ni(12)-In_2O_3. This observation implies a larger contribution of adsorbed formate on In_2O_3 in Ni(12)-Cr(9)-In_2O_3 than in Ni(12)-In_2O_3.

The amount of HCOO* and CH_3O* species under CO_2 hydrogenation conditions (260 °C, 10 bar, 60 min) at a semi-steady state in the IR experiment was estimated by integrating the bands at 2872 and 2931 cm^{-1}, respectively (Fig. 13d and 13e). In our prior IR study on In_2O_3 carried out under identical conditions, the peak areas for formate and methoxy were ~5 and ~3, respectively.[35] Ni(12)-Cr(9)-In_2O_3 displays significantly higher formate and methoxy areas of 10.4 and 7.2, respectively, surpassing values of 8.5 and 5.9 for Cr(10)-In_2O_3, 9.4 and 6.7 for Ni(12)-In_2O_3 and those for In_2O_3. These differences shows that the Ni(12)-Cr(9)-In_2O_3 surface contains more HCOO* and CH_3O* intermediates during the ongoing reaction than Ni(12)-In_2O_3, Cr(10)-In_2O_3 and In_2O_3. The presence of Ni as a hydrogenation promoter can explain the larger amount of reaction intermediates compared to In_2O_3. Based on XRD, XAS and TPR, it can be inferred that Cr decreases the size of In_2O_3 particles and facilitates the formation of O_v on the In_2O_3 surface, thereby enhancing CO_2 adsorption yielding more formate and methoxy intermediates. Overall, these data point to a synergistic effect between Ni and Cr in promoting the formation of formate and methoxy intermediates in methanol formation.

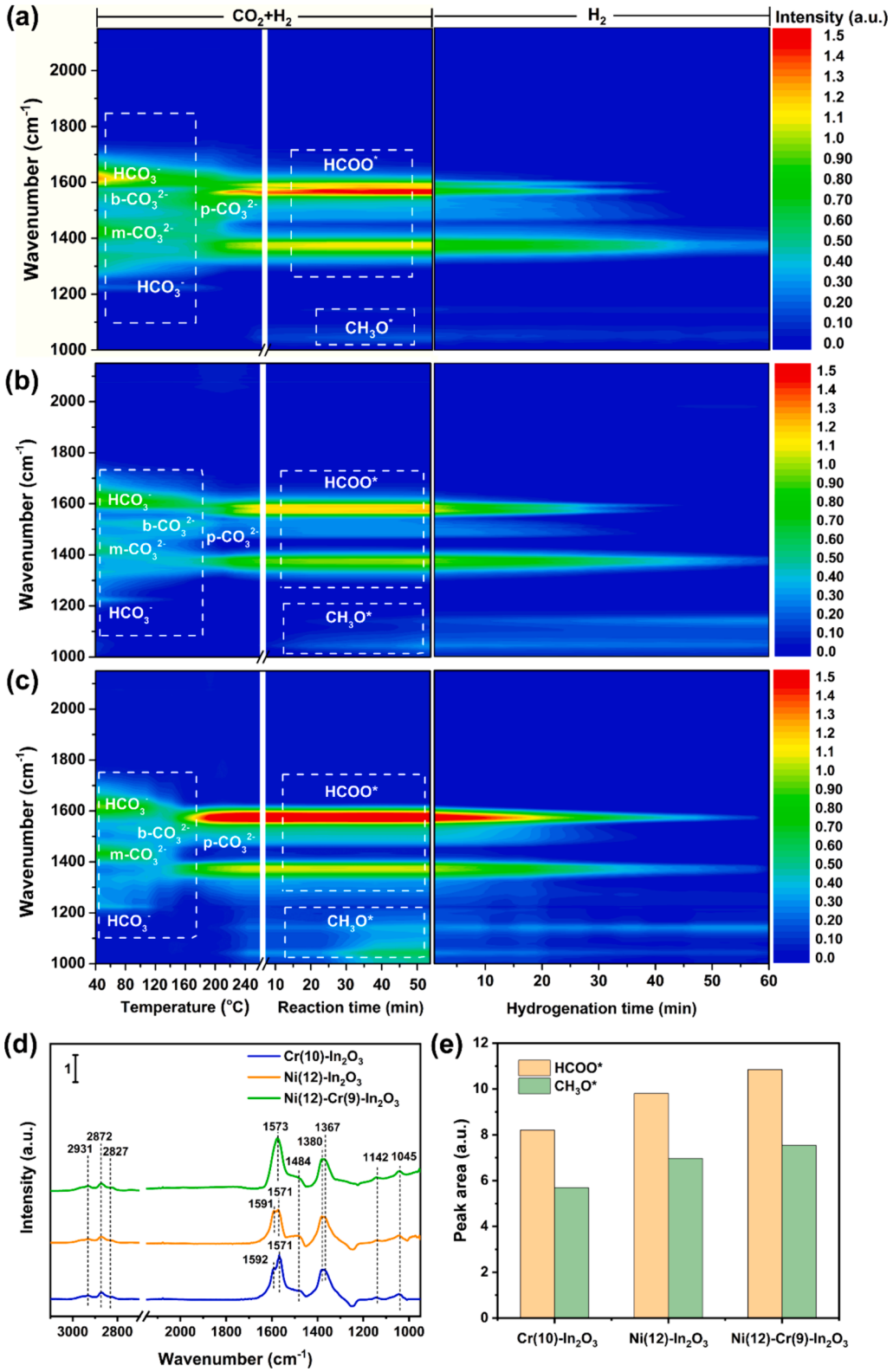

Fig. 13. In situ FTIR spectra as a function of temperature and hydrogenation time over (a) Cr(10)-In_2O_3, (b) Ni(12)-In_2O_3 and (c) Ni(12)-Cr(9)-In_2O_3. (d) FTIR spectra at reaction temperature at 260 °C over Cr(10)-In_2O_3, Ni(12)-In_2O_3 and Ni(12)-Cr(9)-In_2O_3 samples. (e) Comparison of peak area of HCOO* and CH_3O* collected from the spectra at 260 °C under reaction mixture for 1 h over Cr(10)-In_2O_3, Ni(12)-In_2O_3 and Ni(12)-Cr(9)-In_2O_3 samples. Reaction conditions: CO_2:H_2 = 1:3, gas flow rate = 50 mL/min, P = 10 bar. Peak areas of IR spectra are normalized by the weight of catalyst pellet.

4. Conclusion

We synthesized binary In_2O_3-CrO_x and ternary Ni-In_2O_3-CrO_x catalysts via a one-step flame spray pyrolysis method to investigate the promoting role of Cr. For binary In_2O_3-CrO_x samples, the optimal Cr content was 2 mol%, which resulted in a more than 50 % increase in the methanol formation rate at 300 °C compared to In_2O_3. While the CO_2 conversion rates were similar at higher Cr content, the methanol selectivity decreased. Characterization of these samples and complimentary DFT calculations demonstrated that (i) doping of Cr into the In_2O_3 can lead to more O_v sites, explaining the increased performance at low Cr content, and (ii) Cr-oxide clusters destabilize nearby O atoms in the In_2O_3 surface sites, thereby also increasing the O_v site density and offsetting the decrease in O_v due to coverage of the In_2O_3 surface by Cr-oxide. Cr_2O_3 formed above 2 mol% Cr suppressed the sintering of In_2O_3 during CO_2 hydrogenation, which was especially evident at the higher reaction temperature of 300 °C. The methanol rates of the ternary catalysts containing Ni were further enhanced as compared to Cr-In_2O_3 reference catalysts. The methanol formation rate correlated strongly with the Ni content, an optimum being reached at a Ni content of 22 mol % and a Cr content of 8 mol%. The resulting Ni(22)-Cr(8)-In_2O_3 catalyst displayed twice the methanol rate of a Ni(22)-In_2O_3 reference. Also with Ni promoter, Cr suppressed sintering of In_2O_3 and, thereby, catalyst deactivation. Overall, the results indicate that Ni and Cr play separate promoting roles in achieving an increased and more stable rate of methanol formation compared to In_2O_3: Ni promotes the hydrogenation of formate and methoxy surface intermediates to methanol, while Cr results in more O_v sites and suppresses sintering of In_2O_3.

CRediT authorship contribution statement

Liang Liu: Writing – original draft, Visualization, Validation, Methodology, Investigation. **Francesco Cannizzaro:** Investigation. **Anouar Kaychouhi:** Investigation. **Nikolay Kosinov:** Writing – review & editing, Supervision, Investigation. **Emiel J.M. Hensen:** Writing – review & editing, Funding acquisition, Funding acquisition, Conceptualization.

Declaration of competing interest

The authors declare that they have no known competing financial interests or personal relationships that could have appeared to influence the work reported in this paper.

Data availability

Data will be made available on request.

Acknowledgments

The authors acknowledge NWO and SurfSARA for providing access to computational resources used to carry out the DFT calculations reported in this work. This work was supported by the Netherlands Center for Multiscale Catalytic Energy Conversion (MCEC), an NWO Gravitation program funded by the Ministry of Education, Culture and Science of the government of the Netherlands. This project has received funding from the European Union's Horizon 2020 research and innovation program under the Marie Skłodowska-Curie grant agreement No 801359. We acknowledge Dr. Carlo Marini for the assistance in using the CLÆSS beamline at ALBA Synchrotron under proposal No. 2022025616. We acknowledge MAX IV Laboratory for time on beamline SPECIES-RIXS under proposal no. 20220299. Research conducted at MAX IV, a Swedish national user facility, is supported by the Swedish Research council under contract 2018-07152, the Swedish Governmental Agency for Innovation Systems under contract 2018-04969, and Formas under contract 2019-02496.

Appendix A. Supplementary data

Supplementary data to this article can be found online at https://doi.org/10.1016/j.cej.2024.153204.

References

[1] P. Falkowski, R.J. Scholes, E. Boyle, J. Canadell, D. Canfield, J. Elser, N. Gruber, K. Hibbard, P. Högberg, S. Linder, F.T. Mackenzie, B. Moore III, T. Pedersen, Y. Rosenthal, S. Seitzinger, V. Smetacek, W. Steffen, The global carbon cycle: a test of our knowledge of earth as a system, Science 290 (2000) 291–296, https://doi.org/10.1126/science.290.5490.291.

[2] A. McFarlan, Techno-economic assessment of pathways for electricity generation in northern remote communities in Canada using methanol and dimethyl ether to replace diesel, Renew. Sustain. Energy Rev. 90 (2018) 863–876, https://doi.org/10.1016/j.rser.2018.03.076.

[3] A. González-Garay, M.S. Frei, A. Al-Qahtani, C. Mondelli, G. Guillén-Gosálbez, J. Pérez-Ramírez, Plant-to-planet analysis of CO_2-based methanol processes, Energy Environ. Sci. 12 (2019) 3425–3436, https://doi.org/10.1039/C9EE01673B.

[4] G.A. Olah, Beyond oil and gas: the methanol economy, Angew. Chem. Int. Ed. 44 (2005) 2636–2639, https://doi.org/10.1002/anie.200462121.

[5] J.T. Sun, I.S. Metcalfe, M. Sahibzada, Deactivation of Cu/ZnO/Al_2O_3 methanol synthesis catalyst by sintering, Ind. Eng. Chem. Res. 38 (1999) 3868–3872, https://doi.org/10.1021/ie990078s.

[6] M. Behrens, Promoting the Synthesis of Methanol: Understanding the Requirements for an Industrial Catalyst for the Conversion of CO_2, Angew. Chem. Int. Ed. 55 (2016) 14906–14908, https://doi.org/10.1002/anie.201607600.

[7] O. Martin, A.J. Martín, C. Mondelli, S. Mitchell, T.F. Segawa, R. Hauert, C. Drouilly, D. Curulla-Ferré, J. Pérez-Ramírez, Indium oxide as a superior catalyst for methanol synthesis by CO_2 hydrogenation, Angew. Chem. Int. Ed. 55 (2016) 6261–6265, https://doi.org/10.1002/anie.201600943.

[8] J. Ye, C. Liu, D. Mei, Q. Ge, Active oxygen vacancy site for methanol synthesis from CO_2 hydrogenation on In_2O_3(110): A DFT study, ACS Catal. 3 (2013) 1296–1306, https://doi.org/10.1021/cs400132a.

[9] A. Tsoukalou, P.M. Abdala, D. Stoian, X. Huang, M.-G. Willinger, A. Fedorov, C. R. Müller, Structural evolution and dynamics of an In_2O_3 catalyst for CO_2 hydrogenation to methanol: an operando XAS-XRD and In Situ TEM study, J. Am. Chem. Soc. 141 (2019) 13497–13505, https://doi.org/10.1021/jacs.9b04873.

[10] T. Pinheiro Araújo, J. Morales-Vidal, T. Zou, R. García-Muelas, P.O. Willi, K. M. Engel, O.V. Safonova, D. Faust Akl, F. Krumeich, R.N. Grass, C. Mondelli, N. López, J. Pérez-Ramírez, Flame spray pyrolysis as a synthesis platform to assess metal promotion in In_2O_3-catalyzed CO_2 hydrogenation, Adv. Energy Mater. 12 (2022) 2103707, https://doi.org/10.1002/aenm.202103707.

[11] J. Zhu, F. Cannizzaro, L. Liu, H. Zhang, N. Kosinov, I.A.W. Filot, J. Rabeah, A. Brückner, E.J.M. Hensen, Ni–In synergy in CO_2 hydrogenation to methanol, ACS Catal. 11 (2021) 11371–11384, https://doi.org/10.1021/acscatal.1c03170.

[12] F. Cannizzaro, E.J.M. Hensen, I.A.W. Filot, The promoting role of Ni on In_2O_3 for CO_2 hydrogenation to methanol, ACS Catal. 13 (2023) 1875–1892, https://doi.org/10.1021/acscatal.2c04872.

[13] F. Cannizzaro, S. Kurstjens, T. van den Berg, E.J.M. Hensen, I.A.W. Filot, A computational study of CO_2 hydrogenation on single atoms of Pt, Pd, Ni and Rh on In_2O_3(111), Catal. Sci. Technol. 13 (2023) 4701–4715, https://doi.org/10.1039/D3CY00222E.

[14] C. Yang, C. Pei, R. Luo, S. Liu, Y. Wang, Z. Wang, Z.-J. Zhao, J. Gong, Strong electronic oxide-support interaction over In_2O_3/ZrO_2 for highly selective CO_2 hydrogenation to methanol, J. Am. Chem. Soc. 142 (2020) 19523–19531, https://doi.org/10.1021/jacs.0c07195.

[15] X. Zhang, A.V. Kirilin, S. Rozeveld, J.H. Kang, G. Pollefeyt, D.F. Yancey, A. Chojecki, B. Vanchura, M. Blum, Support effect and surface reconstruction in In_2O_3/m-ZrO_2 catalyzed CO_2 hydrogenation, ACS Catal. 12 (2022) 3868–3880, https://doi.org/10.1021/acscatal.2c00207.

[16] M. Zhu, I.E. Wachs, Iron-Based Catalysts for the High-Temperature Water-Gas Shift (HT-WGS) Reaction: A Review, ACS Catal. 6 (2016) 722–732, https://doi.org/10.1021/acscatal.5b02594.

[17] M.I. Ariëns, V. Chlan, P. Novák, L.G.A. van de Water, A.I. Dugulan, E. Brück, E.J. M. Hensen, The role of chromium in iron-based high-temperature water-gas shift catalysts under industrial conditions, Appl. Catal. B 297 (2021) 120465, https://doi.org/10.1016/j.apcatb.2021.120465.

[18] M. Costa, Toxicity and carcinogenicity of Cr(VI) in animal models and humans, Crit. Rev. Toxicol. 27 (1997) 431–442, https://doi.org/10.3109/10408449709078442.

[19] S. Wang, P. Wang, Z. Qin, W. Yan, M. Dong, J. Li, J. Wang, W. Fan, Enhancement of light olefin production in CO_2 hydrogenation over In_2O_3-based oxide and SAPO-34 composite, J. Catal. 391 (2020) 459–470, https://doi.org/10.1016/j.jcat.2020.09.010.

[20] E.K. Athanassiou, R.N. Grass, W.J. Stark, Chemical aerosol engineering as a novel tool for material science: from oxides to salt and metal nanoparticles, Aerosol Sci. Technol. 44 (2010) 161–172, https://doi.org/10.1080/02786820903449665.

[21] R. Koirala, S.E. Pratsinis, A. Baiker, Synthesis of catalytic materials in flames: opportunities and challenges, Chem. Soc. Rev. 45 (2016) 3053–3068, https://doi.org/10.1039/C5CS00011D.

[22] G. Kresse, D. Joubert, From ultrasoft pseudopotentials to the projector augmented-wave method, Phys. Rev. B 59 (1999) 1758–1775, https://doi.org/10.1103/PhysRevB.59.1758.

[23] J.P. Perdew, K. Burke, M. Ernzerhof, Generalized gradient approximation made simple, Phys. Rev. Lett. 77 (1996) 3865–3868, https://doi.org/10.1103/PhysRevLett.77.3865.

[24] G. Kresse, J. Hafner, Ab initio molecular-dynamics simulation of the liquid-metal–amorphous-semiconductor transition in germanium, Physical Review B 49 (1994) 14251–14269, https://doi.org/10.1103/PhysRevB.49.14251.

[25] G. Kresse, J. Furthmüller, Efficiency of ab-initio total energy calculations for metals and semiconductors using a plane-wave basis set, Comput. Mater. Sci 6 (1996) 15–50, https://doi.org/10.1016/0927-0256(96)00008-0.

[26] D. Albani, M. Capdevila-Cortada, G. Vilé, S. Mitchell, O. Martin, N. López, J. Pérez-Ramírez, Semihydrogenation of acetylene on indium oxide: proposed single-ensemble catalysis, Angew. Chem. Int. Ed. 56 (2017) 10755–10760, https://doi.org/10.1002/anie.201704999.

[27] G. Henkelman, B.P. Uberuaga, H. Jónsson, A climbing image nudged elastic band method for finding saddle points and minimum energy paths, J. Chem. Phys. 113 (2000) 9901–9904, https://doi.org/10.1063/1.1329672.

[28] D. Heidrich, W. Quapp, Saddle points of index 2 on potential energy surfaces and their role in theoretical reactivity investigations, Theor. Chim. Acta 70 (1986) 89–98, https://doi.org/10.1007/BF00532206.

[29] C. Shen, K. Sun, Z. Zhang, N. Rui, X. Jia, D. Mei, C.-J. Liu, Highly Active Ir/In_2O_3 Catalysts for Selective Hydrogenation of CO_2 to Methanol: Experimental and Theoretical Studies, ACS Catal. 11 (2021) 4036–4046, https://doi.org/10.1021/acscatal.0c05628.

[30] H. Zhu, X. Wang, F. Yang, X. Yang, Template-free, surfactantless route to fabricate $In(OH)_3$ monocrystalline nanoarchitectures and their conversion to In_2O_3, Crystal Growth & Design 8 (2008) 950–956, https://doi.org/10.1021/cg700850e.

[31] A.A. Salaeva, M.A. Salaev, G.V. Mamontov, Effect of Cu modifier on the performance of CrO_x/Al_2O_3 catalysts for isobutane dehydrogenation, Chem. Eng. Sci. 215 (2020) 115462, https://doi.org/10.1016/j.ces.2019.115462.

[32] M. Mohammadtaheri, Q. Yang, Y. Li, J. Corona-Gomez, The effect of deposition parameters on the structure and mechanical properties of chromium oxide coatings deposited by reactive magnetron sputtering, Coatings 8 (2018) 111, https://doi.org/10.3390/coatings8030111.

[33] W.F. Chu, A. Rahmel, The kinetics of the reduction of chromium oxide by hydrogen, Metall. Trans. B 10 (1979) 401–407, https://doi.org/10.1007/BF02652512.

[34] V. Muravev, A. Parastaev, Y. van den Bosch, B. Ligt, N. Claes, S. Bals, N. Kosinov, E. J.M. Hensen, Size of cerium dioxide support nanocrystals dictates reactivity of highly dispersed palladium catalysts, Science 380 (2023) 1174–1179, https://doi.org/10.1126/science.adf9082.

[35] L. Liu, B. Mezari, N. Kosinov, E.J.M. Hensen, Al promotion of In_2O_3 for CO_2 hydrogenation to methanol, ACS Catal. (2023) 15730–15745, https://doi.org/10.1021/acscatal.3c04620.

[36] H. Wang, M. Zhang, Q. Lv, Removal Efficiency and Mechanism of Cr(VI) from Aqueous Solution by Maize Straw Biochars Derived at Different Pyrolysis Temperatures, Water 11 (2019) 781, https://doi.org/10.3390/w11040781.

[37] J. Stoch, J. Gablankowska-Kukucz, The effect of carbonate contaminations on the XPS O 1s band structure in metal oxides, Surf. Interface Anal. 17 (1991) 165–167, https://doi.org/10.1002/sia.740170308.

[38] V.R. Moreira, Y.A.R. Lebron, M.M. da Silva, L.V. de Souza Santos, R.S. Jacob, C.K. B. de Vasconcelos, M.M. Viana, Graphene oxide in the remediation of norfloxacin from aqueous matrix: simultaneous adsorption and degradation process, Environ. Sci. Pollut. Res. 27 (2020) 34513–34528, https://doi.org/10.1007/s11356-020-09656-6.

[39] M. Li, W. Luo, A. Züttel, Near ambient-pressure X-ray photoelectron spectroscopy study of CO_2 activation and hydrogenation on indium/copper surface, J. Catal. 395 (2021) 315–324, https://doi.org/10.1016/j.jcat.2021.01.010.

[40] K.H.L. Zhang, Y. Du, P.V. Sushko, M.E. Bowden, V. Shutthanandan, S. Sallis, L.F. J. Piper, S.A. Chambers, Hole-induced insulator-to-metal transition in $La_{1-x}Sr_xCrO_3$ epitaxial films, Phys. Rev. B 91 (2015) 155129, https://doi.org/10.1103/PhysRevB.91.155129.

[41] J. Xue, X. Zhu, Y. Zhang, W. Wang, W. Xie, J. Zhou, J. Bao, Y. Luo, X. Gao, Y. Wang, L.-Y. Jang, S. Sun, C. Gao, Nature of conduction band tailing in hydrogenated titanium dioxide for photocatalytic hydrogen evolution, ChemCatChem 8 (2016) 2010–2014, https://doi.org/10.1002/cctc.201600237.

[42] F. Frati, M.O.J.Y. Hunault, F.M.F. de Groot, Oxygen K-edge X-ray absorption spectra, Chem. Rev. 120 (2020) 4056–4110, https://doi.org/10.1021/acs.chemrev.9b00439.

[43] C. Qiu, Y. Odarchenko, Q. Meng, S. Xu, I. Lezcano-Gonzalez, P. Olalde-Velasco, F. Maccherozzi, L. Zanetti-Domingues, M. Martin-Fernandez, A.M. Beale, Resolving the effect of oxygen vacancies on Co nanostructures Using Soft XAS/X-PEEM, ACS Catal. 12 (2022) 9125–9134, https://doi.org/10.1021/acscatal.2c00611.

[44] V.E. Zhivulin, D.P. Sherstyuk, O.V. Zaitseva, N.A. Cherkasova, D.A. Vinnik, S. V. Taskaev, E.A. Trofimov, S.V. Trukhanov, S.I. Latushka, D.I. Tishkevich, T. I. Zubar, A.V. Trukhanov, Creation and Magnetic Study of Ferrites with Magnetoplumbite Structure Multisubstituted by Al^{3+}, Cr^{3+}, Ga^{3+}, and In^{3+} Cations, Nanomaterials 12 (2022) 1306, https://doi.org/10.3390/nano12081306.

[45] X. Jia, K. Sun, J. Wang, C. Shen, C.-J. Liu, Selective hydrogenation of CO_2 to methanol over Ni/In_2O_3 catalyst, J. Energy Chem. 50 (2020) 409–415, https://doi.org/10.1016/j.jechem.2020.03.083.

[46] N. Rui, Z. Wang, K. Sun, J. Ye, Q. Ge, C.-J. Liu, CO_2 hydrogenation to methanol over Pd/In_2O_3: effects of Pd and oxygen vacancy, Appl. Catal., B 218 (2017) 488–497, https://doi.org/10.1016/j.apcatb.2017.06.069.

[47] E.H.P. Cordfunke, R.J.M. Konings, W. Ouweltjes, The standard enthalpy of formation of In_2O_3, J. Chem. Thermodynam. 23 (1991) 451–454, https://doi.org/10.1016/S0021-9614(05)80132-6.

[48] S.E. Ziemniak, L.M. Anovitz, R.A. Castelli, W.D. Porter, Thermodynamics of Cr_2O_3, $FeCr_2O_4$, $ZnCr_2O_4$, and $CoCr_2O_4$, J. Chem. Thermodynam. 39 (2007) 1474–1492, https://doi.org/10.1016/j.jct.2007.03.001.

[49] M.S. Frei, M. Capdevila-Cortada, R. García-Muelas, C. Mondelli, N. López, J. A. Stewart, D. Curulla Ferré, J. Pérez-Ramírez, Mechanism and microkinetics of methanol synthesis via CO_2 hydrogenation on indium oxide, J. Catal. 361 (2018) 313–321, https://doi.org/10.1016/j.jcat.2018.03.014.

[50] M. Yang, J. Yu, A. Zimina, B.B. Sarma, L. Pandit, J.-D. Grunwaldt, L. Zhang, H. Xu, J. Sun, Probing the Nature of Zinc in Copper-Zinc-Zirconium Catalysts by Operando Spectroscopies for CO_2 Hydrogenation to Methanol, Angew. Chem. Int. Ed. 62 (2023), https://doi.org/10.1002/anie.202216803 e202216803.

[51] R. Ye, L. Ma, J. Mao, X. Wang, X. Hong, A. Gallo, Y. Ma, W. Luo, B. Wang, R. Zhang, M.S. Duyar, Z. Jiang, J. Liu, A Ce-CuZn catalyst with abundant Cu/Zn-OV-Ce active sites for CO_2 hydrogenation to methanol, Nat. Commun. 15 (2024) 2159, https://doi.org/10.1038/s41467-024-46513-3.

[52] Y. Li, W. Xu, W. Liu, S. Han, P. Cao, M. Fang, D. Zhu, Y. Lu, High-performance thin-film transistors with aqueous solution-processed NiInO channel layer, ACS Appl. Electron. Mater. 1 (2019) 1842–1851, https://doi.org/10.1021/acsaelm.9b00377.

[53] M.L. Peterson, G.E. Brown, G.A. Parks, C.L. Stein, Differential redox and sorption of Cr (III/VI) on natural silicate and oxide minerals: EXAFS and XANES results, Geochim. Cosmochim. Acta 61 (1997) 3399–3412, https://doi.org/10.1016/S0016-7037(97)00165-8.

[54] T. Watanabe, K. Ikeda, M. Katayama, Y. Inada, In-situ XAFS study for calcination process of Cr catalyst supported on γ-Al_2O_3 and SiO_2, J. Phys. Conf. Ser. 712 (2016) 012073, https://doi.org/10.1088/1742-6596/712/1/012073.

[55] M.S. Frei, C. Mondelli, R. García-Muelas, J. Morales-Vidal, M. Philipp, O. V. Safonova, N. López, J.A. Stewart, D.C. Ferré, J. Pérez-Ramírez, Nanostructure of nickel-promoted indium oxide catalysts drives selectivity in CO_2 hydrogenation, Nat. Commun. 12 (2021) 1960, https://doi.org/10.1038/s41467-021-22224-x.

[56] C. Schild, A. Wokaun, A. Baiker, On the mechanism of CO and CO_2 hydrogenation reactions on zirconia-supported catalysts: a diffuse reflectance FTIR study: Part II. Surface species on copper/zirconia catalysts: implications for methanoi synthesis selectivity, J. Mol. Catal. 63 (1990) 243–254, https://doi.org/10.1016/0304-5102(90)85147-A.

[57] A.R. Richard, M. Fan, Low-pressure hydrogenation of CO_2 to CH_3OH using Ni-In-Al/SiO_2 catalyst synthesized via a phyllosilicate precursor, ACS Catal. 7 (2017) 5679–5692, https://doi.org/10.1021/acscatal.7b00848.

[58] I.C.t. Have, J.J.G. Kromwijk, M. Monai, D. Ferri, E.B. Sterk, F. Meirer, B. M. Weckhuysen, Uncovering the reaction mechanism behind CoO as active phase for CO_2 hydrogenation, Nat. Commun. 13 (2022) 324, https://doi.org/10.1038/s41467-022-27981-x.

[59] T.-Y. Chen, C. Cao, T.-B. Chen, X. Ding, H. Huang, L. Shen, X. Cao, M. Zhu, J. Xu, J. Gao, Y.-F. Han, Unraveling highly tunable selectivity in CO_2 hydrogenation over bimetallic In-Zr oxide catalysts, ACS Catal. 9 (2019) 8785–8797, https://doi.org/10.1021/acscatal.9b01869.

[60] P.A.U. Aldana, F. Ocampo, K. Kobl, B. Louis, F. Thibault-Starzyk, M. Daturi, P. Bazin, S. Thomas, A.C. Roger, Catalytic CO_2 valorization into CH_4 on Ni-based ceria-zirconia. Reaction mechanism by operando IR spectroscopy, Catal. Today 215 (2013) 201–207, https://doi.org/10.1016/j.cattod.2013.02.019.